Three different glacier surges at a spot: What satellites observe and what not

Frank Paul[1], Livia Piermattei[2], Desiree Treichler[2], Lin Gilbert[3], Luc Girod[2], Andreas Kääb[2], Ludivine Libert[4], Thomas Nagler[4], Tazio Strozzi[5], Jan Wuite[4]

1 Department of Geography, University of Zurich, 8057 Zurich, Switzerland
2 Department of Geosciences, University of Oslo, P.O. Box 1047, 0316 Oslo, Norway
3 UCL-MSSL, Department of Space and Climate Physics, Mullard Space Science Laboratory, Holmbury St Mary, Surrey RH5 6NT, UK
4 ENVEO IT GmbH, Fürstenweg 176, 6020 Innsbruck, Austria
5 Gamma Remote Sensing, 3073 Gümligen, Switzerland

Corresponding author: Frank Paul (frank.paul@geo.uzh.ch)

Abstract

In the Karakoram, dozens of glacier surges occurred in the past two decades, making the region one of its global hotspots. Detailed analyses of dense time series from optical and radar satellite images revealed a wide range of surge behaviour in this region: from slow advances longer than a decade at low flow velocities to short, pulse-like advances over one or two years with high velocities. In this study, we present an analysis of three currently surging glaciers in the central Karakoram: North and South Chongtar Glaciers and an unnamed glacier referred to as NN9. All three glaciers flow towards the same small region but differ strongly in surge behaviour. A full suite of satellites (e.g. Landsat, Sentinel-1 and 2, Planet, TerraSAR-X, ICESat-2) and digital elevation models (DEMs) from different sources (e.g. SRTM, SPOT, HMA-DEM) are used to (a) obtain comprehensive information about the evolution of the surges from 2000 to 2021 and (b) to compare and evaluate capabilities and limitations of the different satellite sensors for monitoring relatively small glaciers in steep terrain. A strongly contrasting evolution of advance rates and flow velocities is found, though the elevation change pattern is more similar. For example, South Chongtar Glacier had short-lived advance rates above 10 km y^{-1}, velocities up to 30 m d^{-1} and surface elevations increased by 200 m. In contrast, the neighbouring and three times smaller North Chongtar Glacier had a slow and near linear increase of advance rates (up to 500 m y^{-1}), flow velocities below 1 m d^{-1} and elevation increases up to 100 m. The even smaller glacier NN9 changed from a slow advance to a full surge within a year, reaching advance rates higher than 1 km y^{-1}. It

FP 25 4 22 9:45 PM
Style Definition: Normal

FP 25 4 22 9:45 PM
Formatted: Font color: Black

FP 25 4 22 9:45 PM
Formatted: Body

FP 25 4 22 9:45 PM
Deleted: satellite sensors

seems that, despite a similar climatic setting, different surge mechanisms are at play and a transition from one mechanism to another can occur during a single surge. The sensor inter-comparison revealed a high agreement across sensors for deriving flow velocities, but limitations are found on small and narrow glaciers in steep terrain, in particular for Sentinel-1. All investigated DEMs have the required accuracy to clearly show the volume changes during the surges and elevations from ICESat-2 ATL03 data fit neatly to the other DEMs. We conclude that the available satellite data allow for a comprehensive observation of glacier surges from space when combining different sensors to determine the temporal evolution of length, elevation and velocity changes.

FP 25 4 22 9:45 PM
Deleted: ATL06

1. Introduction

Glacier surges in the Karakoram are widespread (e.g. Sevestre and Benn, 2015) and have been thoroughly documented using historic literature sources and time series of satellite images (Copland et al., 2011; Bhambri et al., 2017; Paul, 2020). A large number of publications provide insights into decadal elevation changes (e.g. Bolch et al., 2017; Berthier and Brun, 2019; Brun et al., 2017; Gardelle et al., 2013; Rankl and Braun, 2016; Zhou et al., 2017) and mean annual flow velocities (e.g. Dehecq et al., 2015; Rankl et al., 2014) at a regional scale. Using various satellite datasets, several studies have also investigated individual glacier surges at high temporal resolution (e.g. Bhambri et al., 2020; Mayer et al., 2011; Paul et al., 2017; Quincey et al., 2015; Round et al., 2017; Steiner et al., 2018).

FP 25 4 22 9:45 PM
Deleted: provides

This increasing interest is in part due to the hazard potential of glacier surges, in particular when river damming creates lakes that might catastrophically drain in so-called glacier lake outburst floods (GLOFs) with far reaching impacts (e.g. Bazai et al., 2021; Bhambri et al., 2019 and references therein; Iturrizaga, 2005), but also due to the increased availability of satellite data for characterizing surges in detail (e.g. Dunse et al., 2015; King et al., 2021; Nuth et al., 2019; Rashid et al., 2020; Wang et al., 2021; Willis et al., 2018). The still limited understanding of surges in the Karakoram region (e.g. Farinotti et al., 2020) and the high diversity of observed surge characteristics (e.g. Bhambri et al., 2017; Hewitt, 2007; Paul, 2015; Quincey at al., 2015) also contribute to the recent efforts. These studies found that both main types of glacier surges can be found in the Karakoram, sometimes side-by-side: The Alaska type, which might be triggered by a change in the basal hydrologic regime, creates pulse-like surges of a short duration (2-3 years), whereas the thermally-controlled Svalbard type has often active surge durations of many years (e.g. Jiskoot, 2011; Murray et al., 2002; Raymond, 1987; Sharp, 1988). Although the physical reasons for the differences and variability of surges in the Karakoram are yet unknown (e.g. glacier properties, thermal regime, mass balance history), many glaciers in the Karakoram have surged repeatedly, sometimes at surprisingly constant intervals and over centuries (e.g. Bhambri et al., 2017; Paul,

2020). On average, surges in the central Karakoram repeat after 40 to 60 years, but intervals can range from less than 20 to more than 80 years.

In the thermally controlled case, it is sometimes difficult to distinguish a regular advance from a surge, as the transition can be gradual (Lv et al., 2020). Whether an advance (stimulated by a positive mass budget) is indeed a surge might be determined by comparison with the behaviour of neighbouring glaciers. As thresholds on advance rates or ice flow speedup might not be efficient to distinguish (slow) surges from advances in the Karakoram, the typical mass redistribution pattern of a surge (from an upper reservoir to a lower receiving zone) as obtained from differencing digital elevation models (DEMs) acquired a few years apart (e.g. Gardelle et al., 2013) is a more reliable identifier (Lv et al., 2019; Goerlich et al., 2020). Usually, the surface in the upper regions of a glacier does not lower significantly during a regular advance (Lv et al., 2020). A further method to discriminate surges from a usual advance is related to a strong increase in crevassing and development of shear margins. However, these are only visible in very high-resolution satellite images or time-series of SAR data (Leclercq et al., 2021).

In this study, we present (a) a comparative analysis of the on-going surges of three glaciers in the central Karakoram: North and South Chongtar Glacier and a small, unnamed glacier referred to here as NN9. We present a comparative analysis of their changes in length, advance rates, flow velocities and surface elevations to elucidate the respective similarities and differences in surge behaviour. As a second aim of this study, we (b) investigate the feasibility of various satellite sensors and DEMs to follow the temporal evolution of the surges comprehensively. Included are optical (Sentinel-2, Landsat, Planet cubesats) and synthetic aperture radar (SAR) imaging sensors (Sentinel-1, TerraSAR-X), altimeter data from ICESat-2 and DEMs from the Shuttle Radar Topography Mission (SRTM), the Satellite Pour l'Observation de la Terre (SPOT), the High Mountain Asia DEM (HMA-DEM) and the Advanced Spaceborne Thermal Emission and reflectance Radiometer (ASTER). The latter is an external dataset provided by Hugonnet et al. (2021).

FP 25 4 22 9:45 PM
Deleted:)

2. Study region

The study region is located in the central Karakoram, north of the Baltoro Glacier, at about 35.94° N and 76.33° E (Fig. 1). East of the study region stands the second highest mountain in the world, the 8611 m high K2. Slopes of the surrounding terrain are very steep and snow avalanches from the surrounding rock walls are a major source of glacier nourishment. Mass changes over the past 20 years derived from satellite data using the geodetic method show more or less constant near-zero mass budgets in the study region (Hugonnet et al., 2021), confirming the continuation of the 'Karakoram Anomaly' (i.e. the balanced mass budgets) in this region (Farinotti et al., 2020).

FP 25 4 22 9:45 PM
Deleted: 5

Fig. 1: Overview study region

Most precipitation in the study region is brought by westerly air flow during winter, but the monsoon brings moist air from the southeast also during summer (Maussion et al., 2014), falling as snow at the high elevations of the rock walls surrounding most glaciers. However, due to the good protection from nearly all directions, the amount of snowfall in the study region is limited and a dry-continental climate can be expected (e.g. Sakai et al., 2015). As surge-type glaciers are abundant (Copland et al., 2011; Bhambri et al., 2017) and repeat intervals are comparably short (Paul, 2020), several glaciers in the Karakoram are typically actively surging at any given time.

The three glaciers investigated here (North/South Chongtar, NN9) have mean elevations around 5500 m and are surrounded by mountain ridges with elevations between 6000 and 7500 m above sea level. South Chongtar Glacier (shortened to South Chongtar in the following) is the largest with an area of ~31 km^2 and a length of more than 14 km at minimum extent, but it has a narrow tongue with a near-constant width of about 800 m. The glacier is mainly east-west oriented in its upper part, bending towards south-north near the terminus. North Chongtar lies north of South Chongtar and is connected to it in its accumulation area. It flows from southeast to northwest, covers an area of ~10 km^2, has a length of 4.5 km at minimum extent and is about 400 m wide. The unnamed glacier NN9 is located on the opposite side of the main valley and flows roughly from west to east. The glacier is about 3.5 km long at minimum extent with an area of 4 km^2 and a ~300 m wide tongue. Table 1 summarises further characteristics and topographic properties.

Table 1: Basic properties of the three investigated glaciers

At their historically recorded maximum extent the three glaciers reach Sarpo Laggo Glacier, a compound-basin valley glacier with a size of 122.3 km^2. This glacier experienced a massive surge shortly before 1960 (Paul, 2020) and a smaller, more internal one (i.e. not reaching the terminus), between 1993 and 1995 (e.g. Paul, 2015; Bhambri et al., 2017). According to Paul (2020), South Chongtar had a rapid advance during a surge that started in 1966 with a short active phase of about two years followed by a quiescent phase with continuous down-wasting and retreat. During this surge it partly compressed the ice from Sarpo Laggo and deformed a moraine from the Moni Glacier tributary (see Fig. 1), leaving an impressive surge mark. In contrast, North Chongtar started advancing about 55 years ago but has not yet reached Sarpo Laggo. The Shipton map from 1937 (Shipton, 1938) shows North Chongtar in contact with it, indicating that the terminus might reach it again. The glacier NN9 had its last surge from about 1961 to 1971 (leaving a small surge mark on Sarpo Laggo) and retreated in its quiescent phase until 2000, when it started to advance slowly. The two glaciers to the south of NN9 (NN7 and NN8 in Paul, 2020) both surged around 1955, and

again in 1998 and 1980, respectively. NN8 also surged after 2002, indicating a surge cycle of only 20-25 years. The next surge of NN8 can thus be expected in a few years, at least if environmental conditions prevail.

3. Datasets

In this section, we describe the satellite and auxiliary datasets used to derive time series of glacier outlines, surface flow velocities and elevation changes in the study region. Figure 2 shows the temporal coverage of each dataset, and the periods selected for the analysis. Changes in glacier extent have been mapped for the active (advance) phases of the three glaciers, starting with Landsat Multispectral Scanner (MSS) images from 1973 for North Chongtar Glacier. The earliest datasets used to derive flow velocities and elevation changes were acquired in 2000, based on the Landsat 7 Enhanced Thematic Mapper plus (ETM+) panchromatic band and the SRTM DEM, respectively.

Fig. 2: Timeline of datasets used

3.1 Glacier extent and centrelines

We used glacier outlines from the updated Glacier Area Mapping for Discharge from the Asian Mountains (GAMDAM2) inventory by Sakai (2019) as a starting point for all glacier extents. This dataset was locally improved (removing rock outcrops and seasonal snow) using a Landsat 8 image acquired on 21 October 2020 (Fig. 1). Given the unknown final length of the glaciers, we digitized likely maximum extents for the three glaciers, avoiding overlapping polygons in their terminus regions. The virtual extents were guided by maximum extents of previous surges described by Paul (2020).

Changes in extent were derived from time series of spatially consistent Landsat data (MSS, TM, ETM+ and Operational Land Imager (OLI)) from path-row 148-35. The slightly shifted Sentinel-2 scenes (sensor Multi Spectral Imager, MSI) from tile 43SFV were used to bridge a gap in availability of cloud-free Landsat scenes after February 2021. The shift of about 50 m was manually subtracted to obtain a correct time series of length changes. The spatial resolution of the optical sensors used for this purpose is 60 m (MSS), 30 m (TM), 15 m (ETM+, OLI) and 10 m (MSI). The list of satellite scenes used for determination of geometric changes (outlines, length changes) is given in Table S1 of the Supplemental Material.

The centrelines for NN9, South and North Chongtar were manually digitized starting from the highest points of each glacier down to the virtual maximum extent. The centrelines were divided

FP 25 4 22 9:45 PM
Deleted: soon

FP 25 4 22 9:45 PM
Deleted: possible virtual

FP 25 4 22 9:45 PM
Deleted: as well as a couple of

FP 25 4 22 9:45 PM
Deleted:) required

FP 25 4 22 9:45 PM
Deleted: sparse

into equidistant points of 100 m at which values for velocity and elevation were extracted.

3.2. Flow velocity

Time series of optical and SAR data were used to derive glacier flow fields (see Table S2). Landsat 7 and 8 scenes, Sentinel-2 and TerraSAR-X (TSX) were used (Fig. 2) to determine pre-surge flow velocities of South Chongtar and advance/surge phase velocities for all glaciers. Images from Planet cubesats were used for a comparison of results with Sentinel-2 and some gap filling in the time series rather than for a full documentation of the active surge of South Chongtar. The related optical images were acquired in summer or autumn for the pre-surge phase of South Chongtar and all year during its surge (Table S2).

From TSX co-registered single-look slant range complex (SSC) images acquired in StripMap mode, with across- and along-track resolution of up to 3 m are used. The selected image pairs are from two different tracks, cover the study region in the descending direction and were acquired in winter 2011, autumn 2012 and spring 2014 (Table S2). The three SAR image pairs from TSX were acquired in winter, autumn and spring. Time series of Sentinel-1 single-look complex (SLC) data acquired in interferometric wide (IW) swath mode were used to test its feasibility to derive flow velocities and to create an animation of the surge that is unobstructed by clouds. The Sentinel-1 IW SLC data have a nominal ground resolution of 5 m x 20 m.

3.3 Elevation information

To follow elevation changes of the glaciers before and during the surge, we analysed several DEMs from both optical and SAR sensors (Table 2). We used the following DEMs with known acquisition dates: The SRTM1 DEM at 1 arcsec (~30 m) resolution from February 2000 (USGS, 2017), a SPOT5-HRS DEM from October 2010 (Gardelle et al., 2013; we used their version v2 for rugged areas), a SPOT6 DEM from October 2015 (Berthier and Brun, 2019), and a SPOT7-derived DEM from October 2020 that was generated for this study. In addition, we used the HMA-DEM mosaic (Shean, 2017) as a reference for DEM co-registration analysis due to its superior spatial resolution and accuracy over stable terrain (off-glacier) compared to the other DEMs (Fig. S1). The HMA-DEM is composed of various DEM datasets mostly acquired during 2015 (Feb., April, July, and Aug.) in this region. Elevation values along the centrelines are extracted from these DEMs and DEM differences are calculated for the periods 2000-2010, 2010-2015 and 2015-2020. For comparison, we also analysed elevation changes derived from ASTER time series by Hugonnet et al. (2021). These provide additional information about the periods 2000-2004 and 2005-2009 (full calendar years) as well as from 2000 to 2019, before the surge of South Chongtar.

Table 2: Overview DEM characteristics

FP 25 4 22 9:45 PM
Deleted: listed in

FP 25 4 22 9:45 PM
Deleted: Velocities from Landsat 8 were also compared with Sentinel-2.

FP 25 4 22 9:45 PM
Deleted: January

FP 25 4 22 9:45 PM
Deleted: 2005

FP 25 4 22 9:45 PM
Deleted: 2010 period

FP 25 4 22 9:45 PM
Deleted: (

FP 25 4 22 9:45 PM
Deleted:).

We also analysed whether altimetry data from ICESat-2 could be used to reveal elevation changes at a higher temporal resolution. The Advanced Topographic Laser Altimeter System (ATLAS) instrument on-board ICESat-2 acquires elevation profiles at a 91-day temporal resolution since October 2018. Each satellite overpass results in three beam pairs that are separated by 3.3 km and 90 m between/within pairs, respectively (Markus et al., 2017). The ICESat-2 ATL06 dataset provides geolocated land ice surface heights with 40 m spatial resolution in profile direction. Figure S2 shows the ATL06 dates and elevations of data points crossing North and South Chongtar, and the two closest repeating pairs of tracks on South Chongtar. Due to the systematic off-pointing at mid-latitudes, ICESat-2 tracks are not repeated exactly in our study area and the ATL06 data alone proved too sparse, both geographically and temporally, for further analysis of the surges.

The ICESat-2 ATL03 Global Geolocated Photon Data (Neumann et al., 2021), from which the ATL06 dataset is a higher-level derivative, provides surface elevation measurements from individual photons every 0.7 m along the elevation profiles, revealing details of the surface topography of the glaciers. The ICESat-2 surface elevations fall into the time gap of the DEMs between 2015 and 2020, thus providing additional temporal information on the surge development. In total, we found 42 intersections with the centrelines of the three investigated glaciers: 23 on South Chongtar (from seven dates), 13 on North Chongtar (from six dates), and 6 on NN9 (from three dates).

4. Methods

4.1 Glacier extent

The timing of the selected images used to digitize glacier extents varies strongly depending on the advance rates. To have at least a two-pixel change in frontal position (which is sufficient for sound change detection), it varies from several years for the slow advance of North Chongtar to about 16 days for the surge phase of South Chongtar. For North Chongtar also the spatial resolution of the sensor matters to some extent, as two pixels translate to a required advance of 120 and 60 m for MSS and TM, respectively. Due to frequent cloud cover, different scenes had to be used for the individual glaciers (Table S1). For the digitization, the polygon referring to the virtual maximum extent of each glacier was split into a multi-polygon by digitizing the smaller extents visible on the respective satellite images.

FP 25 4 22 9:45 PM
Deleted: ,

Length changes between two terminus positions from t_1 and t_2 were derived manually using the distance tool in ArcGIS. Several values were obtained for each change and a suitable average assigned (values usually varied by about ±10 m). We only used the Landsat 7 and 8 time series for this as the Landsat Collection 1 data had a spatial shift compared to Sentinel-2 (e.g. Paul et al., 2016). The length change values from t_1 to t_2 were divided by the temporal difference ($t_2 - t_1$), converted to mean annual advance rates and assigned to the date that is halfway between t_1 and t_2.

Cumulative changes were obtained by summing up the individual length changes.

4.2 Velocities

Flow velocities typically span two to three orders of magnitude, e.g. from <0.1 m d^{-1} for near stagnant glaciers to >10 m d^{-1} during a surge. When using offset-tracking (e.g. Strozzi et al., 2002) When using offset-tracking (e.g. Strozzi et al., 2002) for both Sentinel-1 and TSX or image correlation for optical data (Debella-Gilo and Kääb, 2012), this range can to some extent be accounted for by varying the search window size or the time between the acquisition dates of the image pair. If glaciers with very different flow velocities are in the study region, it might be required to use images from different dates for the analysis or an adaptive search window (Debella-Gilo and Kääb, 2012). In the following, we describe some basics of the processing lines applied for optical and SAR sensors.

FP 25 4 22 9:45 PM
Deleted: Strozzi et al., 2002)

FP 25 4 22 9:45 PM
Formatted: Font color: Black

The normalized cross-correlation algorithm implemented in the correlation image analysis software (CIAS, Kääb and Vollmer, 2000) is used to calculate the glacier surface displacement between optical satellite image pairs (Fig. S3 is illustrating the workflow). The satellite images were not co-registered as we assume that they are corrected for topographic distortion, and therefore the displacement calculated between two images is the actual horizontal displacement without any influence of topography. To check co-registration, abundant stable terrain was included in the correlation. The displacements are estimated at a spatial resolution of 100 m while the size of the search area is set in relation to the maximum displacement estimated between two satellite scenes. Dividing the displacement by the temporal difference between the image pairs (Table S2) gives velocity in m d^{-1}.

With optical data, clouds, cast shadows and changes in snow cover lead to false detections or biased measurements of the calculated displacement fields. These mismatches are removed in post-processing by setting a threshold of the maximum correlation coefficient (<0.5) and velocity. For Sentinel-2 data, elevated objects such as clouds are detected by applying CIAS between band 4 and band 8 of the same Sentinel-2 scene. The calculated perspective displacements (both bands are recorded at slightly different positions of the sensor) are then used to mask the clouds. For all satellite data, spatial filtering based on a moving median window as well as temporal filtering are applied to remove additional outliers and noise (Fig. S3).

Surface flow velocities for TSX data were derived by an iterative offset-tracking technique developed for SAR data (Wuite et al., 2015). This method does not require coherence and is thus also capable of acquiring flow velocity data over longer time spans and in regions with fast flow. The method is based on cross-correlation of templates in SAR amplitude images and provides both the along-track and line-of-sight velocity components from a single image pair. We used a template

size of 96×96 pixels for generating velocity maps with 50 m grid spacing and applied a 9x9 inverse-distance median filter in the post-processing step to remove outliers and fill in small gaps. For Sentinel-1, the same method was applied but tests with various image template sizes were performed with an image pair acquired on 4. and 16. November 2020 during the peak of the surge (Fig. S4).

4.3 Elevation data

We used the MicMac software to generate the SPOT 2020 DEM from the raw imagery (Rupnik et al., 2017). The pre-processing of all DEMs follows the standard processing steps for DEM differencing. All DEMs were projected to UTM 43N (EPSG 32643), elevations were vertically transformed to the WGS 84 ellipsoid and DEMs were co-registered to the HMA DEM using OPALS (Pfeifer et al., 2014). Specifically, we applied least squares matching to estimate the full 3D affine transformation parameters that minimize the errors with respect to the reference DEM over common stable areas. These were manually digitized off-glacier excluding slope values larger than 40 degrees (Fig. S5). Because of data voids, we also had to exclude large parts of the accumulation areas of some glaciers in the case of the SPOT 2010 and 2015 DEMs.

All DEMs were resampled, clipped and aligned to the same 30 m grid and a high-resolution 5 m grid for the HMA DEM and SPOT 2020. We did not correct the SRTM DEM for microwave penetration into ice and snow (Gardelle et al., 2012), as the effect is small compared to the elevation differences caused by the surges and uncertain, i.e. it is not systematic and any for example elevation dependent correction can not be justified either. Elevation values were extracted along the centrelines and subtracted from SRTM.

To estimate volume changes resulting from the surges, volume gain and loss (i.e., summing up all positive and negative values within the tongues) were calculated for each glacier tongue with adjusted extents and glacier-specific epochs (Fig. S5). For comparison, we included the glaciers NN7 and NN8 (see Fig. 1) in the analysis as they also surged during the study period.

As the ICESat-2 ATL06 datasets did not provide useful results, only the ATL03 dataset was further processed using python libraries geopandas (Jordahl et al., 2021), rasterio (Gillies et al., 2021) and shapely (Gillies et al., 2021a). The photon elevations were filtered to only retain elevation samples classified as likely land or ice surfaces (parameters signal_conf_ph / signal_conf_ph_landice >1) and classified into glacier and off-glacier samples using maximum glacier outlines. On the bright glacier surface, both the weak and strong laser beams yield sufficient photon returns for complete elevation profiles. This is less true for moraines / rocky areas (profile 3 in Fig. S6), where the weak beam yields considerably fewer surface returns.

FP 25 4 22 9:45 PM
Deleted: 1611.

FP 25 4 22 9:45 PM
Deleted: .

FP 25 4 22 9:45 PM
Deleted: We also excluded

FP 25 4 22 9:45 PM
Deleted: from further analyses. This removes

FP 25 4 22 9:45 PM
Deleted: DEMs, but had little impact for the other

FP 25 4 22 9:45 PM
Deleted: and uncertain

FP 25 4 22 9:45 PM
Deleted: /

Elevation values were sampled for all elevation points (containing a DEM cell) and the AMES stereo pipeline (version 2.7.0, Shean et al., 2016) was used to co-register the elevation profiles (only off-glacier samples) with the already co-registered DEMs used in this study (no co-registration offset was found). The profiles were intersected with the glacier centrelines to compare the ATL03 elevation samples with the DEMs. The median of all elevation samples on each profile within a 10 m buffer from the centreline are used as surface elevations at the intersection points.

4.4 Uncertainties

The uncertainty of the length change data has been determined by measuring for each glacier and each time step different points at the terminus. From the range of values, a reasonable mean value was determined manually. Glacier terminus positions were digitized only once and used only for a qualitative illustration (outline overlay) of the changes, i.e. we have not explicitly calculated uncertainties of glacier extents. As a range of sensors with different spatial resolutions is used for the digitizing (e.g. Landsat MSS, ETM+, OLI and Sentinel-2), the uncertainty varies with the sensor.

Based on the assumption that measurement errors over glaciers and other terrain are common (Paul et al., 2017), we assessed the uncertainties of glacier flow velocities from stable terrain velocity observations, where flow velocities are supposed to be zero, using the same stable areas as used for DEM co-registration (Fig. S5). Uncertainties are derived as measures of median and a robust standard deviation based on the median absolute deviation (MAD), which is a bit less sensitive to outliers (e.g. Dehecq et al., 2015). Co-registration accuracy of the DEMs was computed from elevation differences calculated over stable terrain (off glacier) with slopes smaller than 40° (Fig. S5).

5. Results

5.1 Changes in glacier extent and morphology

In Fig. 3 the temporal evolution of terminus positions is depicted as an overlay of extents showing slow advances of NN9 (starting in 2000) and North Chongtar (since 1973) along with a rapid advance of South Chongtar (starting mid-2020). For better visibility, the retreat phase of South Chongtar from 2000 to mid-2020 is not shown. Snapshots of the geometric evolution can be found in Fig. S7 for the time period before the surge of South Chongtar (1993-2019) and in Fig. S8 for the time during its surge (2020-2021). The related cumulative length changes for all three glaciers are shown in Fig. 4a for their advance phases, whereas Fig. 4b only shows advance rates for the glaciers NN9 and North Chongtar (they were out of scale for South Chongtar).

Fig. 3: Multi-temporal outline overlay advance phase

South Chongtar entered its quiescent phase after its 1966/67 surge and exhibited constant thinning with limited frontal retreat over several decades. After 30 years (in 2000) the former surge lobe was still largely ice filled, though increasingly debris covered. Driven by further thinning, a clear retreat of the terminus (remaining clean ice) became visible after 2000, reaching about -800 m by 2009 and -2300 m by mid-2020. During this retreat phase, its middle part always showed some residual flow, i.e. it was not completely stagnant. In 1993 a deformation of the medial moraine started moving forward, about 300 m by 2009 and 500 m by 2019.

In 2017, a new surge developed with the typical funnel-shaped appearance of the front. While the lowest part of the glacier was still thinning and retreating in 2019, the surge front reached the terminus in July 2020 and the front started advancing by about 3 km in 10 months (Fig. 4a) with advance rates of up to 12.6 km yr^{-1} (35 m d^{-1}) in early Nov. 2020. During this time the lower part widened massively and the entire surface became heavily crevassed. The front advanced into its former surge mark on Sarpo Laggo Glacier and pushed the ice surrounding it towards the opposite side of the valley. By June 2021 advance rates decreased considerably, but the terminus was still advancing.

Fig. 4: Cumulative length changes and advance rates

North Chongtar on the other hand, advanced at a more or less constant rate of 30 m y^{-1} until 2004 when it passed a total of 800 m since 1973 (earliest MSS image, see Table S1). A very high-resolution satellite image from 2001 is available in Google Earth and shows some crevassing near the terminus but not a surging glacier. There is no indication of a melt water stream leaving the glacier snout. After 2005, advance rates increased linearly and we assign this as the onset of the surge phase. This increase resulted in a nearly completely crevassed surface and widespread shear margins. Both are also visible in the 15 m resolution Landsat panchromatic bands, and, even better, in very high-resolution images from 2011 and 2016 available in Google Earth. In 2013 the terminus reached a step in the valley slope, creating a deep transverse crevasse that seemed to separate the lowest part of the tongue but actually didn't. By 2021 nearly the entire surface was still crevassed and the glacier had advanced by a further 1600 m since 2004, i.e. 2.4 km in total.

The small valley **glacier NN9** slowly retreated until 1998 and started advancing a year later at about a constant rate of 40 m y^{-1} until 2016 (Fig. 4). Up to this year, its lowest parts had some crevasses but looked otherwise like a usual advancing glacier. This changed a year later when the glacier thickened considerably, developed shear margins and started advancing at a much higher rate of up to 1000 m y^{-1} in 2021, indicating the start of the surge phase. The increasingly crevassed surface also became visible in Sentinel-2 images and with the 15 m Landsat 8 band. The total ad-

vance from 1999 to 2018 was 800 m followed by a further 500 m until June 2021. In July the frontal advance accelerated further reaching nearly 3 km y^{-1} in August 2021, whereby the lower part of the tongue separated from the main glacier and slid down the remaining kilometre in about a month. More ice is following from higher elevations, possibly leading to some interaction with the still advancing terminus of South Chongtar.

5.2 Flow velocities

5.2.1 NN9 and North Chongtar

Selected flow velocity maps for the two glaciers are shown in Fig. 5 and related velocity profiles along the centreline of the main trunk can be seen in Figs. 6a and b for NN9 and North Chongtar, respectively. The c. 300-400 m wide tongue of NN9 is at the edge of the possibilities for deriving flow velocities with offset-tracking (and a 100 m grid) from the optical sensors, but the high resolution of TSX StripMap acquisitions provides near-complete spatial coverage (Fig. 5b). Due to local cloud cover several of the optical image pairs selected for South Chongtar could not be used for NN9 and North Chongtar.

Though scattered, the values derived from Landsat 7 (Fig. 5a), Sentinel-2 (Fig. 5c) and Landsat 8 (Fig. 5d) look reasonable. Pre-surge values are around 0.1 m d^{-1} with Landsat 7 (2000-2002) and TSX (2011 and 2012) and a bit higher (up to 0.2 m d^{-1}) with Sentinel-2 in 2017 (Fig. 6a). Afterwards values in the lower part of NN9 (between 2.5 and 4 km) start increasing to 0.4 m d^{-1}, reaching 0.8 m d^{-1} between August and October 2020. The upper glacier started accelerating in autumn 2020 with a near-linear increase up to the terminus (Fig. 6a), indicating surge activation in the lower part of the glacier. The increased crevassing of NN9 is also visible in the higher intensity values of the Sentinel-1 animation towards the latest images (see Supplemental Material).

Fig. 5: 2D flow velocity maps 2000-2019 for all glaciers

For the larger North Chongtar, a slightly better coverage can be obtained from the optical sensors than for NN9. The most homogenous flow fields are derived by TSX (Fig. 5b) indicating higher flow velocities of up to 0.4 m d^{-1} in its lower two thirds up to the terminus in 2012. The profiles in Fig. 6b from Landsat 7 show similar values. Velocities derived from Sentinel-2 between 2016 and 2019 are lower in the region from 3 to 5.5 km. There is a zone with very low velocities between 4.5 and 5 km and acceleration further down. From August 2019 to October 2020 flow velocities are between 0.8 and 1 m d^{-1} near the terminus, indicating that this region is fast flowing and advancing, whereas the upper regions are still moving with 0.2 to 0.4 m d^{-1}.

FP 25 4 22 9:45 PM
Deleted: .

FP 25 4 22 9:45 PM
Deleted: afterwards

Fig. 6: 1D centre-line velocity profiles NN9 & South Chongtar

5.2.2 South Chongtar

The much larger South Chongtar glacier was adequately captured by the optical sensors so that a more continuous flow field could be derived (Fig. 5) and pre-surge flow evolution could be followed in detail (Fig. 7a). Comparing the maps in Fig. 5, a slow but steady increase of flow velocities from 2000 to mid-2019 over large parts of the glacier can be seen, starting at about 0.15 m d^{-1} and ending at 0.4 m d^{-1}. These values are similar to the other two glaciers, but affect a larger region. The temporal evolution shown in Fig. 7a confirm this observation, pre-surge flow velocities are highest (up to 0.4 m d^{-1}) near the middle of the glacier (around 8 to 10 km) and decrease gradually to 0 m d^{-1} at its highest and lowest points. In the region between 11 and 14 km the gradual increase of flow velocities can be followed from 2000/02 (with Landsat 7) to 2014 (with TSX). Mean annual values with Landsat 8 from 2013 to 2014 match perfectly with mean monthly TSX values from April to May 2014. Landsat 8 velocities from 2013 to 2016 and Sentinel-2 from 2016 to 2019 show the continuation of the slow velocity increase over the entire glacier length, reaching 0.4 m d^{-1} in 2018/19. A direct comparison with Landsat 8 over nearly the same period (grey dots in Fig. 7a) is shown on top of the curve from Sentinel-2, indicating again a near-perfect match. In August 2019 the gradual increase changed at first rapidly to 0.8 m d^{-1} and then more slowly to 1.1 m d^{-1} between September 2019 and June 2020. With the stagnant terminus still at 13.5 km, the strong velocity increase behind the front marks the onset of the surge around August 2019.

Fig. 7: Velocities South Chongtar

The last curve from Fig. 7a is repeated in Fig. 7b (dark blue at the bottom), as we had to switch the scale for better visibility of velocities during the surge phase. Flow velocities increased to about 4 m d^{-1} by July 2020. In August 2020 we could derive detailed flow fields from Sentinel-2 images acquired only 5 days apart. A sharp surge front with maximum velocities formed, reaching values of more than 25 m d^{-1} in August/September 2020. With peak velocities near 30 m d^{-1} as derived locally from Planet imagery (Fig. S10), South Chongtar Glacier had likely one of the highest flow velocities ever measured in the Karakoram region. Behind this maximum, flow velocities decreased about linearly back to km 3 along the centre line. When the surge front reached the terminus in July 2020, a rapid advance started (see 5.1). Velocities dropped to 15 m d^{-1} by November 2020 and below 10 m d^{-1} by January 2021. Afterwards, maximum velocities are found near km 15 and decreased only slowly at this location and over large parts of the glacier length (back to km 6) at about the same rate, indicating that the active surge was on-going. Around km 10 along the centre line, velocity is still around 5 m d^{-1} in early May 2021 or 40 times higher than during the quiescent phase (Fig. 7b). The related Hovmöller diagram for the surge phase in Fig. 7c confirms the strong pulse-like acceleration in August 2020 with a rapid decline afterwards. The corresponding 2D plots of flow velocities during the surge phase of South Chongtar (Fig. 8) also reveal the rapid velocity increase by September 2020 and the decrease afterwards.

FP 25 4 22 9:45 PM
Deleted: ,

FP 25 4 22 9:45 PM
Deleted: 2

FP 25 4 22 9:45 PM
Deleted: S9

FP 25 4 22 9:45 PM
Deleted: 3

FP 25 4 22 9:45 PM
Deleted: changed

FP 25 4 22 9:45 PM
Deleted: entire

FP 25 4 22 9:45 PM
Deleted: km

Fig. 8: 2D maps of surface velocities South Chongtar

The spatial distribution of highest flow velocities of Figs. 8b and c are not symmetric to the centre line, indicating that the deformation-related maximum flow velocity in the centre of a glacier has reduced relevance here. This somehow counterintuitive behaviour indicates that during a surge basal sliding is the process dominating over deformation. Other possibilities are a decreased resistance of the valley floor or because of the topography redirecting the mass flow from northwest to north. The cross-profile flow velocities (Fig. 9) reveal that this pattern persists throughout the entire surge.

Fig. 9: 1D cross-profile velocities South Chongtar (surge phase)

5.3 Elevation changes

In the three panels of Fig. 10 we show differences in elevation between the SRTM DEM and the other four DEMs along the centrelines of the three glaciers. Additionally, differences from selected ICESat-2 ATL03 points are plotted. Figure 11 shows related elevation change maps for 2000 – 2010, 2010 – 2015, 2015 – 2020 and 2000 – 2020. DEM differences obtained from ASTER in an independent study (Hugonnet et al., 2021) have been used for comparison.

The elevation data for **NN9** (Fig. 10a) show virtually no change in its upper part down to 3.5 km where the terminus was located in 2000. The ICESat-2 data adds no further information here, as all available data points are located in the upper part. Below this region, the 'elevation gain' due to the advancing snout can be followed down to km 4.5 in 2020. The small region of elevation gain by the advancing tongue is also visible in each of the maps in Fig. 11. The elevation differences between the two high-resolution DEMs from 2015 and 2020 in Fig. 11c reveal some surface lowering in the upper part (about 10-15 m), but over the longer period 2000 to 2020 (Fig. 11d) this lowering nearly disappears (i.e. is smaller than the SRTM uncertainty). So for NN9 the typical mass transfer of a surge could not be observed until October 2020 and elevation changes look like expected for a usual advance rather than a surge.

FP 25 4 22 9:45 PM
Deleted: ,

For **North Chongtar** (Fig. 10b) the situation is similar, but a surface lowering of about 40 m can be observed at higher elevation. The SPOT data from October 2015 and ICESat-2 data points from December 2018 at 4.2 km indicate that the largest changes happened between 2015 and 2018. Accordingly, this change is well visible in the high-resolution 2015-2020 DEM difference (Fig. 11c) and the differences over the full 2000-2020 period (Fig. 11d). However, also here the elevation gain in the lower glacier part is comparably localized and largely due to the advance of the terminus.

572
573 *Fig. 10: 1D profile elevation changes compared to SRTM*
574
575 **South Chongtar** shows profiles (Fig. 10c) and surface change patterns (Fig. 11) that are in line
576 with a typical surge, maybe apart from the fact that the thickening of the upper glacier regions is
577 limited. The 2000 to 2010 change map (Fig. 11a) shows a slightly bluish upper part and some arte-
578 facts. Over the longer 2000 to 2015 period the elevation gain from 4 to 12 km is about 20-30 m
579 (Fig. 10c), but further down a significant surface lowering (>50 m) can be observed between 13
580 and 18 km. This lowering is also visible in the 2D map of Fig. 11a, marking at its upper point the
581 position where the active ice starts, i.e. where the surface lowering is compensated by the mass
582 flux. The 2020 surge moved ice between 3 and 8 km towards its lower part between 10 and 16 km,
583 causing a surface elevation decrease of 20-40 m in the reservoir zone and an increase of up to 130
584 m at km 14.
585
586 The ICESat-2 data points constrain the surface elevation evolution in time (Fig. 10c): The tongue
587 was still only slightly thicker at 12 km in March 2019, as surface lowering of the upper part (at 5.7
588 km) had not started in February 2020 and the terminus had not advanced by March 2020. Between
589 6 and 14 km we find a smooth linear increase of the elevation differences (Fig. 10c) - but the ICE-
590 Sat-2 data points at 9.5 km show a slight surface lowering between December 2019 and August
591 2020, indicating that the surge front passed this part of the glacier already before the end of August
592 2000. The 2015 to 2020 elevation change map (Fig. 11c) reveals that elevation changes mostly
593 occurred over this time period. Due to the opposite elevation change pattern before 2015, elevation
594 changes over the full period 2000-2020 are less pronounced. The constantly down-wasting Sarpo
595 Laggo Glacier in the valley floor shows an elevation loss of up to 100 m over this period.
596
597 *Fig. 11: 2D elevation change maps*
598
599 **5.4 Volume changes**
600 In Table 3 the results of the calculated volume changes are listed, differentiated for the gain and
601 loss part. They add some quantitative information over a larger part of the glacier surface (see Fig.
602 S5). With the timing of the DEMs not always synchronous with the start/end of a surge, the calcu-
603 lated values can be underestimated due to the overlap of surge phases. For example, the volume
604 gain in the lower part of South Chongtar from 2000 to 2020 includes the volume loss between
605 2000 and 2019. For this reason we only analyse the 2015 to 2020 changes for South Chongtar
606
607 For NN9 no mass transfer from an upper region is found. We have a near zero mass loss compared
608 to a clear volume gain of 0.03 km^3. For the continuous advance/surge of North Chongtar the vol-
609 ume gain is a bit higher than the loss resulting in a small overall volume gain over the full 20-year

period (Fig. 11d). However, Fig. 11c reveals that compensation effects are included: Between 2015 and 2020 some of the volume gain from the period before has already started thinning. The volume gain part for South Chongtar is about 10 times higher compared to North Chongtar and NN9. However, there is also considerable volume loss at higher elevations compensating about half of the gain. To put just the volume gains of these five glaciers (+0.46 km^3) into perspective, the (uncompensated) volume loss of Sarpo Laggo Glacier over the full period (-0.47 km^3) is the same.

Table 3: Volume changes

5.5 Uncertainty assessment

5.5.1 Glacier length changes

Uncertainties of the length changes are estimated to be in the order of one image pixel, i.e. 60 m for MSS, 30 m for TM, 15 m for OLI pan and 10 m for Sentinel-2. As frontal advances have only been measured for a change of at least 3 to 4 pixels, the given values should be well outside the uncertainty range in most cases. However, the calculated frontal advance rates for glacier NN9 and North Chongtar (Fig. 4b) show fluctuations. These can be attributed to the measurement uncertainties so that in reality the increase might have been smoother and more gradual. There is thus some caution to not over-interpret the details of the change rates.

5.5.2 Flow velocities

The displacements measured by Landsat over the selected stable areas show median values close to the expected value of 0 m d^{-1}, with a MAD between 0.01 and 0.04 m d^{-1}, as reported in Table S2. Among the Landsat data, Landsat 7 shows the smallest standard deviation based on the MAD. For Sentinel-2, the uncertainties of the displacement on stable terrain are lower for the pairs with a time interval of approximately a year. For these pairs, the median and the MAD of the velocity are of the same order of magnitude as the Landsat results. For shorter time intervals (5 to 45 days), the Sentinel-2 velocity shows medians between 0.15 and 1.58 m d^{-1} with a maximum MAD of 1.39 m d^{-1}. Displacement from Planet data gives the largest error with medians and MAD values ranging from 0.3 m d^{-1} to 2.50 m d^{-1}. One pair showed a significantly higher error with a median value of 8.64 m d^{-1} and a corresponding MAD value of 4.76 m d^{-1}, which is in a similar order of magnitude to the displacement measured in the centre line of the glacier (13.89 m d^{-1}). TSX revealed the lowest uncertainty with values of both median and MAD close to 0 m d^{-1}.

5.5.3 Elevation data

The median elevation differences on stable bedrock to the reference DEM (HMA DEM) are 1.02 m (SRTM), 1.03 m (SPOT 2010), -0.12 m (SPOT 2015) and 1.08 m (SPOT 2020), with standard deviations of 3-15 m (Table S3). Also mean elevation differences, which are more sensitive to ex-

FP 25 4 22 9:45 PM
Deleted: .

FP 25 4 22 9:45 PM
Moved (insertion) [1]

FP 25 4 22 9:45 PM
Moved (insertion) [2]

FP 25 4 22 9:45 PM
Moved (insertion) [3]

treme values, are <1.4 m for all DEM difference pairs except for the SPOT 2020-SRTM2000 DEM pair (2.4 ±8.8 m). These are small differences and fully within the range of expected uncertainties (after successful co-registration), considering the very steep and rugged terrain. We found no indication of remaining horizontal shifts between the DEMs (this would be visible as an aspect-dependent pattern in Fig. 11). The comparison of the SPOT 2015 and HMA 2015 DEM (Fig. S13) shows a minor tiling effect caused by the composite nature of the HMA DEM in the upper accumulation areas of North and South Chongtar. The mean uncertainty of the ATL06 ICESat-2 data was ±5.37 m. However, we assume that ATL03 elevation uncertainties are in the order of decimetres on the relatively smooth glacier surface.

5.6 Sensor inter-comparison

5.6.1 Velocities

As can be seen in Fig. 7a, velocity values derived from the (optical) 15 m resolution Landsat 8 panchromatic band for the period July 2018 to July 2019 are about the same as from (also optical) 10 m resolution Sentinel-2 data for the period August 2018 to August 2019. Both lines are basically on top of each other. The same applies to the Landsat 8 velocities for the period September 2016 to October 2017 compared to Sentinel-2 values over the period November 2016 to November 2017. The velocities derived from the (SAR) TSX sensor over the short period April to May 2014 also compare well with the annual mean values from Landsat 8 over the period July 2013 to July 2014. In Fig. S9 we show the related velocity differences with respect to the distance along the centre line for all three comparisons, revealing that they are largely within ±0.03 m d^{-1} for the region between km 9 and the terminus. They are therefore as small as the stable terrain uncertainties listed in Table S2. Between km 0 and 9 only a few values are available for the optical sensors and these are subject to outliers. The differences are thus higher but in most cases still smaller than the flow velocity.

The (optical) Planet cubesat images cover only the lower part of the glacier. Here, the Planet velocity (Fig. S10) reveals the same increase/decrease pattern as the Sentinel-2 velocity profile (Fig. 7b). Direct comparison of the flow velocities reveals much larger differences, but compared to the much higher flow velocities still only small differences (Fig. S11). These can be related to slightly different time intervals and the rapidly changing crevasse pattern at high flow velocities. On the other hand, the differences are large when comparing velocities derived from Sentinel-1 (SAR) with the optical Sentinel-2 (Fig. S12). The large image template sizes of 128 x 64 (450 m x 900 m) for South Chongtar (tongue width 800 m) result in a strong underestimation of Sentinel-1 velocities with errors much greater than those reported in previous studies for larger Arctic glaciers (Paul et al., 2017; Strozzi et al., 2017). The information density is also very low compared to Sentinel-2, indicating that Sentinel-1 data do not reveal sufficient detail about the surge.

FP 25 4 22 9:45 PM
Moved (insertion) [4]

FP 25 4 22 9:45 PM
Deleted: intercomparison

FP 25 4 22 9:45 PM
Deleted: 5

FP 25 4 22 9:45 PM
Deleted: and the average differences are insignificant.

FP 25 4 22 9:45 PM
Deleted: TSX velocities from

FP 25 4 22 9:45 PM
Deleted: compared to

FP 25 4 22 9:45 PM
Deleted: period, the latter curve being on top of TSX in Fig. 7a (apart from the

FP 25 4 22 9:45 PM
Deleted: 8 and

FP 25 4 22 9:45 PM
Deleted: km).

FP 25 4 22 9:45 PM
Deleted: S9

FP 25 4 22 9:45 PM
Deleted: S10) that

FP 25 4 22 9:45 PM
Deleted: . This is different

FP 25 4 22 9:45 PM
Deleted: derived velocities

FP 25 4 22 9:45 PM
Deleted: S11

FP 25 4 22 9:45 PM
Deleted: indicated

FP 25 4 22 9:45 PM
Deleted: density of the

5.6.2 Elevation changes

Of the seven analysed elevation datasets, ICESat-2 elevation profiles show most detail compared to the DEMs and is also resolving small surface features such as crevasses and séracs (Fig. S6). Both the weak and the strong laser beams of ICESat-2's three beam pairs provide equally good data in the snow-covered accumulation areas (Fig. S6a and b). On darker and more rugged surfaces the weak beam yields considerably fewer photon returns than the strong beam (bottom panels in Fig. S6e and f).

Elevation differences between the HMA DEM and the SPOT DEM from 2015 are depicted in Fig. S13. A small advance of North Chongtar and a slight elevation increase on South Chongtar within the few months' time gap is visible. The latter is confirmed by the cross transects in Fig. S6c and d. In contrast, the elevations of the two 2015 DEMs agree very well for the transects in the upper accumulation area (top panels) and the down-wasting tongue in the main valley (bottom panels). Apart from artefacts and local differences in very steep terrain, elevations of the DEMs from 2015 agree very well both on and off glaciers.

The elevation changes derived from the ASTER DEM time series by Hugonnet et al. (2021) shown in Fig. S14 are similar to the time series we analysed from SRTM, SPOT and the HMA DEMs (Fig. 11). The ASTER DEMs have more artefacts and local differences, in particular in very steep terrain. In contrast, the strong spatial filtering inherent in the ASTER dataset, smoothens artefacts and data gaps off and to some degree also details on glaciers. Locally, the ASTER data set is less complete, e.g., the advance of North Chongtar is not well covered and the advance of the glacier NN8 is not visible.

There are no further insights when splitting the 2000-2010 period into a 2000-2004 and 2005-2009 period, but the 2000 to 2019 period from ASTER (Fig. S14f) reveals the up to 40 m elevation increase in the upper region of South Chongtar. This 'reservoir zone' seemingly stretches over the entire upper glacier rather than being an isolated region. In 2019 the surge has not started, so the strong elevation loss in its lower part from post-surge down-wasting of the previous surge is also very prominent. Elevation gain from 2000 to 2019 is also visible for the upper part of Sarpo Laggo Glacier and the lower part of Moni Glacier.

FP 25 4 22 9:45 PM
Deleted: 5

FP 25 4 22 9:45 PM
Deleted: top panels in

FP 25 4 22 9:45 PM
Deleted: S6

FP 25 4 22 9:45 PM
Deleted: S6

FP 25 4 22 9:45 PM
Deleted: S12

FP 25 4 22 9:45 PM
Deleted: the middle panels in

FP 25 4 22 9:45 PM
Deleted: S6

FP 25 4 22 9:45 PM
Deleted: S13

FP 25 4 22 9:45 PM
Deleted: S13f

FP 25 4 22 9:45 PM
Deleted:

FP 25 4 22 9:45 PM
Deleted: 5.6 Uncertainty assessmen ... [1]

FP 25 4 22 9:45 PM
Moved up [1]: .1 Glacier length changes

FP 25 4 22 9:45 PM
Deleted: 5.6

FP 25 4 22 9:45 PM
Moved up [2]: .2 Flow velocities
The displacements measured by Landsat over the selected stable areas show median values close to the expected value of 0 m d^{-1}, with a MAD between 0.01 and 0.04 m d^{-1}, as reported in Table S2. Among the Landsat data, Landsat 7 shows the smallest standard deviation based on the MAD. For Sentinel-2, the uncertainties of the displacement on stable terrain are lower for the pairs with a time interval of approximately a year. For these pairs, the median and the MAD of the velocity are of the same order of magnitude as the Landsat results. For shorter time intervals (5 to 45 days), the Sentinel-2 velocity shows medians between 0.15 and 1.58 m d^{-1} with a maximum MAD of 1.39 m d^{-1}. Displacement from Planet data gives the largest error with medians and MAD values ranging from 0.3 m d^{-1} to 2.50 m d^{-1}. One pair showed a significantly higher error with a median value of 8.64 m d^{-1} and a corresponding MAD value of 4.76 m d^{-1}, which is in a similar order of magnitude to the displacement measured in the centre line of the glacier (13.89 m d^{-1}). TSX revealed the lowest uncertainty with values of both median and MAD close to 0 m d^{-1}.

6. Discussion

6.1 Interpretation of the surges

The contrasting surge behaviour of North and South Chongtar glacier is remarkable in that the two glaciers with probably the highest (South Chongtar) and lowest (North Chongtar) flow velocities and advance rates during a surge (in the entire Karakoram) can be found side-by-side. At first glance, it seems that the sudden, short-lived surge of South Chongtar is hydrologically controlled (Alaska type), whereas the neighbouring North Chongtar surge seems thermally controlled (Svalbard type). However, as Quincey et al. (2015) noted, this simplified picture does not work well for many glacier surges in the Karakoram, which often show characteristics of both types. For example, the South Chongtar surge reached its maximum flow velocities in summer rather than winter and its drop is very slow rather than fast. For a hydrologically controlled surge one would expect a surge start in winter (when efficient basal hydrology switches to inefficient) and a sudden end of the surge in summer (when basal water can again be released efficiently) (e.g. Kamb et al., 1985; Raymond, 1987; Sharp, 1988). Moreover, flow velocities increased slowly, steadily and over large parts of the glacier rather than being located at a clearly localized surge front. These observations fit better with a thermally controlled surge (e.g. Fowler et al., 2001) and imply that both mechanisms apply and the surge mechanism could be named 'hybrid'.

The slow and near constant advance of North Chongtar and NN9 might not even be classified as a surge, but given that both glaciers also developed nearly all characteristics of a surge at some point (e.g. a heavily crevassed surface, shear margins, strong increase in flow velocity, high frontal advance rates, mass transfer from a reservoir to a receiving zone), the former advance phase might be seen as a part of the surge. Still, from the evolution of advance rates or flow velocities alone it is nearly impossible to pin down the exact surge onset for North Chongtar. Morphological changes (heavy crevassing, shear margins) indicate that this might have happened around 2010, but considering the near linear increase of advance rates after 1996, one might assign the onset also to that year. In any case, the more or less constant advance for more than 30 years before 1996 is exceptional and only comparable to the very slow advance of Maedan Glacier in the neighbouring Panmah region that also started in the 1960s, before advance rates considerably increased in the mid-1990s and the glacier started surging (Bhambri et al. 2017; Paul, 2020). Such prolonged advances might also be a consequence of a positive mass balance that one glacier converted to a continuous advance and another one to a surge (Lv et al., 2020). At least the elevation change pattern of North Chongtar over the 2000-2020 period reveals a clear and typical redistribution of mass from a higher reservoir zone to a lower receiving zone.

FP 25 4 22 9:45 PM
Moved up [3]: to the reference DEM (HMA DEM) are 1.02 m (SRTM), 1.03 m (SPOT 2010), -0.12 m (SPOT 2015) and 1.08 m (SPOT 2020), with standard deviations of 3-15 m (Table S3). Also mean elevation differences, which are more sensitive to extreme values, are <1.4 m for all DEM difference pairs except for the SPOT 2020-SRTM2000 DEM pair (2.4 ±8.8 m). These are small differences and fully within the range of expected uncertainties (after successful co-registration), considering the very steep and rugged terrain. We found no indication of remaining horizontal shifts between the DEMs (this would be visible as an aspect-dependent pattern in Fig. 11). The comparison of the SPOT 2015 and HMA 2015 DEM (Fig.

FP 25 4 22 9:45 PM
Deleted: 5.6.3 Elevation data ... [2]

FP 25 4 22 9:45 PM
Moved up [4]:) shows a minor tiling effect caused by the composite nature of the HMA DEM in the upper accumulation areas of North and South Chongtar. The mean uncertainty of the ATL06 ICESat-2 data was ±5.37 m. However, we assume that ATL03 elevation uncertainties are in the order of decimetres on the relatively smooth glacier surface.

FP 25 4 22 9:45 PM
Deleted: S12

FP 25 4 22 9:45 PM
Deleted: as

FP 25 4 22 9:45 PM
Deleted: likely

FP 25 4 22 9:45 PM
Deleted: and

FP 25 4 22 9:45 PM
Deleted: hold

FP 25 4 22 9:45 PM
Deleted: their

FP 25 4 22 9:45 PM
Deleted: constantly

FP 25 4 22 9:45 PM
Deleted: fit to

FP 25 4 22 9:45 PM
Deleted: implies

FP 25 4 22 9:45 PM
Deleted: ,

This is different for NN9, which only shows elevation increase in its lower part over this period without any measurable surface lowering higher up. This rather unique criterion for surge identification fails here and would exclude the glacier from being surge type. However, a different impression emerges when looking at the temporal evolution of advance rates and flow velocities. In 2016 the former increased considerably from about 40 m y^{-1} to more than 1 km y^{-1} and the morphology of the surface changed from rather smooth to highly crevassed. Measurable flow velocities increased in 2019 from 0.2 to 0.8 m y^{-1} and the Landsat 8 image pair from 2018 to 2019 (Fig. 5d) also reveals an increase. With its recent rapid advance, the glacier has now reached its former 1971 maximum extent and also looks the same in terms of a completely crevassed surface (Paul, 2020). The slow advance might have resulted from a positive mass balance but could also be a thermally controlled surge. However, the recent increase in advance rates could also be due to a hydrologically controlled surge and/or due to the steep slope and dynamic effects. Compared to North Chongtar, the switch from advance to surge occurred much more sudden.

For South Chongtar the situation is clearer as its rapid advance and more than 100-fold increase in flow velocities (from 0.2 to more than 25 m/d) is typical for a hydrologically controlled surge with increasing basal water pressure. We assume that its thin lowest part was frozen to the bed (e.g. Obu et al., 2019), effectively blocking water release for some time. The interesting points of the current surge are: (a) the gradual increase of flow velocities in the region above its fixed terminus (at km 13.5), (b) the extreme velocity increase from July to September 2020, (c) the high maximum velocities of 30 m d^{-1}, (d) the location of the maximum away from the centre line, and (e) the more or less constantly high flow velocities over large parts of its length from January to May 2021. The latter is responsible for the ongoing mass transport and advance of the terminus and implies that basically the entire glacier was activated by the surge. As mentioned above, points (a) and (e) are more typical for thermally controlled surges so with both characteristics this surge can be classified as hybrid. That velocities increase from the centre to the boundary of a glacier (Fig. 9) is likely rather unique. We assume this is caused by the surrounding topography, i.e. the change of flow direction from northwest to north imposed by the mountain walls. The centre of the advancing terminus collided with the southern rock wall and was then diverted to a different direction. As the glacier was likely sliding over its full width, the resistance at the boundaries was likely limited.

FP 25 4 22 9:45 PM
Deleted: km

Maximum surface flow velocities of 30 m d^{-1} are only visible with Planet and to the edge of the glacier (Fig. 9), Sentinel-2 values peak at 27 m d^{-1}. This is likely due to the higher resolution of Planet compared to Sentinel-2 and hence to the smaller region used for spatial averaging. Also the shorter time period considered (3 days) might play a role. Whereas high flow velocities of about 15 m d^{-1} have been reported previously (Quincey et al., 2015; Paul et al., 2017; Bhambri et al.,

2020), values above 25 m d^{-1} are only rarely observed in the Karakoram (Rashid et al., 2020). The latter study reports values near 50 m d^{-1} for the last surge of Shispar Glacier (derived from 3 m Planet data), but the flow fields look a bit 'bumpy' and image processing artefacts might have contributed to the high values. We assume that the rapid increase in flow velocities during July/August was due to additional lubrication from summer surface melt water.

In principle, a surge simply moves mass downstream implying that the net volume change should be about zero. However, if surges take place over very long periods (>5 years) there will also be a signal from the usual ablation and accumulation. Moreover, for DEMs derived from optical sensors problems in snow covered or steep terrain (shadow) exists that might create data gaps in the region where the mass has been removed (or where mass gain took place before a surge). Both effects can create biases leading to over- or underestimation of calculated volume changes. These apply also to the changes calculated over ten-year periods and the SPOT DEM from 2010 that had data voids in the steep upper regions of some glaciers. In consequence, volume changes calculated with this DEM are incomplete and need to be interpreted with care. However, as both positive and negative changes take place in regions of increased uncertainty, the net effect is likely small.

6.2 Uncertainties

The one-pixel uncertainty in deriving terminus positions and length changes translates into an uncertainty of the calculated advance rates. How large the uncertainties are, depends on the sensor resolution and the time period between two measurements. It is assumed that at least a part of the short-term variations in the advance rates of NN9 and North Chongtar are due to these uncertainties rather than real variability.

FP 25 4 22 9:45 PM
Moved (insertion) [5]

FP 25 4 22 9:45 PM
Moved (insertion) [6]

With the exception of the Planet data, the uncertainty of the velocity measured over stable terrain by all sensors is one or two orders of magnitude smaller than the maximum displacement observed on the glacier along the centreline, even for the two small glaciers NN9 and North Chongtar. For them, cloud cover has been identified as a major challenge for optical sensors. In fact, the selection of the satellite pair prioritized the reduction of cloud cover on South Chongtar rather than NN9 and North Chongtar, which were rarely cloud-free. Hence, it is not only spatial resolution that is responsible for data limitations.

In general, the uncertainties of glacier flow velocity measurements are mainly related to co-registration accuracy, orthorectification, the time interval between image pairs, surface conditions (shadow, snow, etc.) and the spatial resolution of the images. The larger the time window between two pairs, the smaller the uncertainty of the measured velocity. Despite the higher resolution, the uncertainty is higher for Planet than for Sentinel-2. For Sentinel-2, the orthorectification error is minimized because the imagery comes from the same relative orbit (Kääb et al., 2016). On the

contrary, we have different orbital paths between Planet image pairs and therefore further geometric corrections may be needed to minimize this error, as also suggested by Kääb et al. (2017) and Millan et al. (2019). Also the very small stable terrain uncertainties of TSX are likely due to the accurate co-registration of the image pairs.

The observed elevation changes exceed the DEM elevation uncertainties by an order of magnitude or more, which makes our elevation change analyses very robust. For volume change studies, data gaps in the DEMs and remaining blunders/bias from clouds or other sources cause greater uncertainties than the elevation uncertainties themselves (McNabb et al. 2019). Data gaps occur, however, mostly in the accumulation areas due to reduced contrast over snow, more persistent cloud cover and steeper terrain. Moreover, surface elevation tends to change much less here than it is the case for the tongues, and uncertainties might become as large as the changes. The elevation accuracy of the ICESat-2 ATL03 product is clearly superior to all DEMs analysed within this study.

6.3 Sensor capabilities and limits

The sensor intercomparison revealed a very good agreement between the velocity data derived from both TSX StripMap mode and Sentinel-2 with Landsat 8 (Fig. 7a), as well as between Sentinel-2 and Planet (Fig. S11). This confirms that all three optical sensors can be used to derive the temporal evolution of flow velocities – cloud cover, snow conditions and cast shadow permitting. The key point is the choice of the temporal baseline of image pairs as a function of glacier surface changes, sensor resolution and the targeted velocity field. At 20 m d^{-1} a 5 day interval is equivalent to a change by 10 pixels with Sentinel-2 and 20 pixels with Planet over 3 days (assuming a 3 m resolution). At 0.1 m d^{-1} the displacement is about 35 m (3 Sentinel-2 pixels) after a year, which is at the lower end of what is detectable with offset-tracking.

For SAR data the typical limitations are layover/foreshortening, radar shadow, SAR penetration and decorrelation. Actually, none of these created problems for the TSX and Sentinel-1 image pairs used here. However, Sentinel-1 performed poorly even on the largest glacier, South Chongtar. This was mostly due to the fact that this glacier has a long and narrow tongue (width less than 800 m) situated between steep mountain flanks. Because of the relatively large size needed for the matching window (Fig. S4), too many non-moving off-glacier pixels are included affecting the velocity retrieval considerably (Fig. S12). Also, the large and fast surface changes on the rapidly surging glacier might have changed the backscatter patterns too much to be tracked over time (Strozzi et al., 2017). The minimum width of a glacier to be reliably monitored with Sentinel-1 in the Himalayas is likely around 2 km. On the contrary, TSX yielded dense and consistent velocity values for all three glaciers (pre-surge-phase). As it seems, the map in Fig. 5b captures nicely the flow acceleration of North Chongtar in 2012, which decreased afterwards (Fig. 6b). The much noisier values from Landsat 8 in this figure (compared to Sentinel-2 and TSX) revealed that the 15

FP 25 4 22 9:45 PM
Deleted: S10

FP 25 4 22 9:45 PM
Deleted: (3)

FP 25 4 22 9:45 PM
Deleted: (

FP 25 4 22 9:45 PM
Deleted: in

FP 25 4 22 9:45 PM
Deleted: Unfortunately

FP 25 4 22 9:45 PM
Deleted: ,

FP 25 4 22 9:45 PM
Deleted: it is

FP 25 4 22 9:45 PM
Deleted: relative

FP 25 4 22 9:45 PM
Deleted: S11

FP 25 4 22 9:45 PM
Deleted: reliable

m resolution of the Landsat panchromatic band is seemingly insufficient to track displacements precisely. Note, though, that these comparisons are not strict as the sensors have different resolutions, and the datasets cover different phases of the surges and thus different surface conditions.

The compared DEMs are of similar quality over glaciers, but the SPOT 2010 DEM used by Gardelle et al. (2013) suffered from strong artefacts at steep slopes. The elevation values of the SPOT 2015 and HMA DEM (which is also from 2015 in this region) are basically identical apart from individual raster cells (e.g. showing the advancing terminus of North Chongtar). So elevation changes from 2000 (SRTM) to 2015 (HMA DEM) can also be derived from freely available DEMs. The SPOT 2020 DEM is of superb quality but the raw image pair had to be purchased. For a study looking at specific glaciers this is certainly worthwhile, but does typically hamper larger regions to be covered.

The surface elevation detail and accuracy of the freely available ICESat-2 ATL03 photon data surpasses all other datasets, including the SPOT 2020 DEM (Fig. S6). When combined with one or several DEMs, the higher temporal resolution provides additional information on how the elevation changed in-between DEM time stamps. This may be very useful for slower changes or to further constrain the onset/end of a rapid change, such as a surge. However, ICESat-2 only provides elevation profiles with varying locations, which makes this data type more demanding to analyse. The footprints of the ICESat-2 ATL06 time series alone are too sparse to derive any useful trends in glacier surface elevation.

The DEM time series from ASTER images (Fig. S14) derived by Hugonnet et al. (2021) shows the same trends as from the DEMs used here. They provide further information over the 2000–2005 and 2005–2010 periods, but miss the surge of South Chongtar as they end in 2019. On the other hand, they cover a much larger area and clearly reveal the increase in surface elevation of South Chongtar over the full 2000-2019 period. The coverage of the smaller glaciers is noisier with ASTER than with the DEMs we have used and locally values are missing, but the temporal evolution over several larger glaciers can be well followed. Deriving further DEMs from future ASTER stereo scenes might thus help to determine total volume changes after all surges have come to an end, including the not yet visible volume loss in the reservoir zone of NN9.

FP 25 4 22 9:45 PM
Deleted: strictly

FP 25 4 22 9:45 PM
Deleted: .

FP 25 4 22 9:45 PM
Deleted: S13

FP 25 4 22 9:45 PM
Deleted: not

FP 25 4 22 9:45 PM
Deleted: .. [3]

FP 25 4 22 9:45 PM
Moved up [5]: **Uncertainties** .

FP 25 4 22 9:45 PM
Moved up [6]: in the advance rates of NN9 and North Chongtar are due to these uncertainties rather than real variability. .

With the exception of the Planet data, the uncertainty of the velocity measured over stable terrain by all sensors is one or two orders of magnitude smaller than the maximum displacement observed on the glacier along the centreline, even for the two small glaciers NN9 and North Chongtar. For them, cloud cover has been identified as a major challenge for optical sensors. In fact, the selection of the satellite pair prioritized the reduction of cloud cover on South Chongtar rather than NN9 and North Chongtar, which were rarely cloud-free. Hence, it is not only spatial resolution that is responsible for data limitations. .

In general, the uncertainties of glacier flow velocity measurements are mainly related to co-registration accuracy, orthorectification, the time interval between image pairs, surface conditions (shadow, snow, etc.) and the spatial resolution of the images. The larger the time window between two pairs, the smaller the uncertainty of the measured velocity. Despite the higher resolution, the uncertainty is higher for Planet than for Sentinel-2. For Sentinel-2, the orthorectification error is minimized because the imagery comes from the same relative orbit (Kääb et al., 2016). On the contrary, we have different orbital paths between Planet image pairs and therefore further geometric corrections may be needed to minimize this error, as also suggested by Kääb et al. (2017) and Millan et al. (2019). Also the very small stable terrain uncertainties of TSX are likely due to the accurate co-registration of the image pairs. .

The observed elevation changes exceed the DEM elevation uncertainties by an order of magnitude or more, which makes our elevation change analyses very robust. For volume change studies, data gaps in the DEMs and remaining blunders/bias from clouds or other sources cause greater uncertainties than the elevation uncertainties themselves (McNabb et al. 2019). Data gaps occur, however, m ... [4]

FP 25 4 22 9:45 PM
Deleted: It is assumed that at least a part of the variation

7. Conclusions

We have identified and presented an analysis of three glacier surges in the central Karakoram, all taking place in the same small region but with very different characteristics and possibly forcing mechanisms. South Chongtar showed advance rates of more than 10 km y^{-1}, velocities up to 30 m d^{-1} and surface elevations rose by 200 m all within a surge duration of about 2-3 years. The three times smaller and neighbouring North Chongtar Glacier had a slow and almost-linear increase of advance rates (up to 500 m y^{-1}) over a period of almost 50 years, flow velocities below 1 m d^{-1} and elevation increases of up to 100 m. A more active phase from 2010 to 2015 was followed by a continuation of its slow advance. The even smaller glacier NN9 changed from a slow advance to a full surge within a year, reaching advance rates higher than 1 km y^{-1}, but showing the typical surface lowering higher up only recently. Total length changes reached between 2 and 2.7 km for the three glaciers and the size of NN9 changed by more than 20%. For South Chongtar, maximum flow velocities are found near its southern boundary rather than in the centre.

At first glance, the surge of South Chongtar clearly resembles the classical Alaska type surge (hydrologically controlled), whereas North Chongtar and NN9 better fit to the Svalbard type (thermally controlled). However, the summer onset and slow velocity decay of the South Chongtar surge and the sudden change in frontal advance rates of NN9 hint to the respective other type, resulting in a change of characteristics. North Chongtar has not changed type but surge onset is difficult to determine as advance rates increased linearly, morphological changes developed slowly and a 50-year advance might also be called a surge. When the definition of a surge is stricter, we would assign the surge onset of NN9, North and South Chongtar to 2017, 2005-2010 and August 2019, respectively. We speculate that the thin, lower part of South Chongtar was cold ice frozen to the bed, reducing possibilities for the terminus to advance and causing basal pressure to strongly increase.

The sensor intercomparison revealed that Landsat 8 and Sentinel-2 are difficult to be used jointly for determination of geometric changes as their geolocation differs (>30 m). Flow velocities agreed well across sensors for South Chongtar, except for Sentinel-1 that had problems due to its narrow tongue (800 m). However, the backscatter intensity images provided a time-series of surge evolution at a near constant interval that is undisturbed by clouds. At the two smaller glaciers NN9 and North Chongtar, the optical sensors still provided reasonable and consistent flow velocities, but limits due to spatial resolution and cloud cover became visible (more noise). The TerraSAR-X acquisitions in StripMap mode revealed by far the best results and depicted the surge of North Chongtar accurately.

FP 25 4 22 9:45 PM
Deleted: .

FP 25 4 22 9:45 PM
Deleted: has

FP 25 4 22 9:45 PM
Deleted:),

After proper co-registration, all DEMs provided useful results to track elevation and volume changes, independent of glacier size. The two SPOT DEMs from 2010 and 2015 suffered from artefacts at steep slopes, but the latter compared very well to the HMA-DEM. The high-resolution SPOT6 DEM from Oct 2020 had impressive quality and allowed an accurate calculation of the volume change of all glaciers up to this point in time. The very precise ICESat-2 elevation profiles provided additional information in space (glacier surface details) and time (between the DEMs) that matched well to the other datasets. The ASTER DEM time series missed detecting local changes of smaller glaciers, but provided a larger overview and complementary information on cumulative elevation changes shortly before the surge of South Chongtar started.

All three glaciers are still advancing and South Chongtar and NN9 are now colliding. The bulldozing of the South Chongtar terminus into the down-wasting ice of Sarpo Laggo Glacier is already creating interesting morphological changes. North Chongtar might again reach the floor of the main valley as in the 1930s, but this could take some more years. We conclude that the past and further evolution of these and other glacier surges can be well observed from satellite data, at best by combing all available datasets.

Supplement

The supplement related to this article is available on-line at: TBD

Author contributions

F.P. detected the surges, lead the writing and analysed changes in extent and morphology. L.P. contributed equally, derived the optical velocity data and prepared all related tables and figures; D.T. derived and combined the elevation change data. All authors contributed to the writing, discussion and editing of the text.

Code and data availability

Data processing has been performed using freely available (e.g. CIAS, MicMac, geopandas/rasterio/shapely) or in-house software (for SAR offset-tracking). In addition, most of the datasets used here are freely available (e.g. Landsat, Sentinel-1/-2, ICESat-2, SRTM and HMA DEMs, glacier outlines) or can be obtained with a quota (Planet). TerraSAR-X data were ordered from DLR and the SPOT2020 DEM was purchased from Airbus. The SPOT DEMs from 2010 and 2015 were provided by E. Berthier.

FP 25 4 22 9:45 PM
Deleted: Also

FP 25 4 22 9:45 PM
Deleted: Planet,

FP 25 4 22 9:45 PM
Deleted:), except

FP 25 4 22 9:45 PM
Deleted: (

FP 25 4 22 9:45 PM
Deleted:)

FP 25 4 22 9:45 PM
Deleted: (ordered form

FP 25 4 22 9:45 PM
Deleted:).

Competing interests

The authors declare that they have no conflict of interest.

Acknowledgements

We thank Etienne Berthier for providing the SPOT 2010 and 2015 DEMs and the two anonymous reviewers for providing thorough and constructive reviews, which improved the clarity of the paper. We also acknowledge free access to Sentinel-1 and -2 data from Copernicus, Landsat from USGS, Planet from Planet, the SRTM DEM from USGS, the HMA DEM from NSIDC, and glacier outlines from GLIMS. This study would not have been possible otherwise.

Financial support

This study has been supported by the ESA project Glaciers_cci (grant no. 4000127593/19/I-NB).

FP 25 4 22 9:45 PM
Deleted: This study has been performed in the framework of the ESA project Glaciers_cci (4000127593/19/I-NB).

FP 25 4 22 9:45 PM
Deleted:

References

Bazai, N. A., Cui, P., Carling, P. A., Wang, H., Hassan, J., Liu, D., Zhang, G., and Jin, W.: Increasing glacial lake outburst flood hazard in response to surge glaciers in the Karakoram, Earth-Science Reviews, 212, 103432, https://doi.org/10.1016/j.earscirev.2020.103432, 2021.

Berthier, E. and Brun, F.: Karakoram geodetic glacier mass balances between 2008 and 2016: persistence of the anomaly and influence of a large rock avalanche on Siachen Glacier, J. Glaciol., 65, 494–507, https://doi.org/10.1017/jog.2019.32, 2019.

Bhambri, R., Hewitt, K., Kawishwar, P., and Pratap, B.: Surge-type and surge-modified glaciers in the Karakoram, Sci Rep, 7, 15391, https://doi.org/10.1038/s41598-017-15473-8, 2017.

Bhambri, R., Hewitt, K., Kawishwar, P., Kumar, A., Verma, A., Snehmani, Tiwari, S., and Misra, A.: Ice-dams, outburst floods, and movement heterogeneity of glaciers, Karakoram, Global and Planetary Change, 180, 100–116, https://doi.org/10.1016/j.gloplacha.2019.05.004, 2019.

Bhambri, R., Watson, C. S., Hewitt, K., Haritashya, U. K., Kargel, J. S., Pratap Shahi, A., Chand, P., Kumar, A., Verma, A., and Govil, H.: The hazardous 2017–2019 surge and river damming by Shispare Glacier, Karakoram, Sci Rep, 10, 4685, https://doi.org/10.1038/s41598-020-61277-8, 2020.

Bolch, T., Pieczonka, T., Mukherjee, K., and Shea, J.: Brief communication: Glaciers in the Hunza catchment (Karakoram) have been nearly in balance since the 1970s, The Cryosphere, 11, 531–539, https://doi.org/10.5194/tc-11-531-2017, 2017.

Brun, F., Berthier, E., Wagnon, P., Kääb, A., and Treichler, D.: A spatially resolved estimate of High Mountain Asia glacier mass balances from 2000 to 2016, Nature Geosci, 10, 668–673, https://doi.org/10.1038/ngeo2999, 2017.

Copland, L., Sylvestre, T., Bishop, M. P., Shroder, J. F., Seong, Y. B., Owen, L. A., Bush, A., and Kamp, U.: Expanded and Recently Increased Glacier Surging in the Karakoram, Arctic, Antarctic, and Alpine Research, 43, 503–516, https://doi.org/10.1657/1938-4246-43.4.503, 2011.

Debella-Gilo M., and Kääb, A.: Locally adaptive template sizes for matching repeat images of Earth surface mass movements. ISPRS Journal of Photogrammetry and Remote Sensing, 69, 10-28, https://doi.org/10.1016/j.isprsjprs.2012.02.002, 2012.

Dehecq, A., Gourmelen, N., and Trouve, E.: Deriving large-scale glacier velocities from a complete satellite archive: Application to the Pamir–Karakoram–Himalaya, Remote Sensing of Environment, 162, 55–66, https://doi.org/10.1016/j.rse.2015.01.031, 2015.

Dunse, T., Schellenberger, T., Hagen, J.O., Kääb, A., Schuler, T.V., and Reijmer, C.H.: Glacier-surge mechanisms promoted by a hydro-thermodynamic feedback to summer melt, The Cryosphere, 9, 197–215, https://doi.org/10.5194/tc-9-197-2015, 2015.

Farinotti, D., Immerzeel, W. W., de Kok, R. J., Quincey, D. J., and Dehecq, A.: Manifestations and mechanisms of the Karakoram glacier Anomaly, Nat. Geosci., 13, 8–16,

https://doi.org/10.1038/s41561-019-0513-5, 2020.

Fowler, A.C., Murray, T., and Ng, F.S.L.: Thermally controlled glacier surging. J. Glaciol., 47(159), 527–538, 2001.

Gardelle, J., Berthier, E., and Arnaud, Y.: Impact of resolution and radar penetration on glacier elevation changes computed from DEM differencing, J. Glaciol., 58, 419–422, https://doi.org/10.3189/2012JoG11J175, 2012.

Gardelle, J., Berthier, E., Arnaud, Y., and Kääb, A.: Region-wide glacier mass balances over the Pamir-Karakoram-Himalaya during 1999–2011, Cryosphere, 7, 1263–1286, https://doi.org/10.5194/tc-7-1263-2013, 2013.

Gillies, S. et al.: Rasterio: geospatial raster I/O for Python programmers, Software from https://github.com/ Toblerity/Shapely, 2021a.

Gillies, S. et al.: Shapely: manipulation and analysis of geometric objects, Software from https://github.com/mapbox/rasterio, 2021b.

Goerlich, F., Bolch, T., and Paul, F.: More dynamic than expected: an updated survey of surging glaciers in the Pamir, Earth Syst. Sci. Data, 12, 3161–3176, https://doi.org/10.5194/essd-12-3161-2020, 2020.

Hewitt, K.: Tributary glacier surges: an exceptional concentration at Panmah Glacier, Karakoram Himalaya, J. Glaciol., 53, 181–188, https://doi.org/10.3189/172756507782202829, 2007.

Hugonnet, R., McNabb, R., Berthier, E., Menounos, B., Nuth, C., Girod, L., Farinotti, D., Huss, M., Dussaillant, I., Brun, F., and Kääb, A.: Accelerated global glacier mass loss in the early twenty-first century, Nature, 592, 726–731, https://doi.org/10.1038/s41586-021-03436-z, 2021.

Iturrizaga, L.: New observations on present and prehistorical glacier-dammed lakes in the Shimshal valley (Karakoram Mountains), Journal of Asian Earth Sciences, 25, 545–555, https://doi.org/10.1016/j.jseaes.2004.04.011, 2005.

Jarvis, A., Reuter, H. I., Nelson, A., Guevara, E.: Hole-filled seamless SRTM data V4, International Centre for Tropical Agriculture (CIAT) [dataset], https://srtm.csi.cgiar.org, 2008.

Jiskoot, H.: Glacier surging, in: Encyclopedia of Snow, Ice and Glaciers, edited by: Singh, V. P., Springer, Dordrecht, Netherlands, pp. 415-428.

Jordahl, K., et al.: geopandas / geopandas: v0.9. Software from: http://doi.org/10.5281/zenodo.4569086, 2021.

Kääb, A. and Vollmer, M.: Surface geometry, thickness changes and flow fields on creeping mountain permafrost: automatic extraction by digital image analysis. Permafrost Periglac, 11, 315-326, https://doi:10.1002/1099-1530(200012)11:4<315::AID-PPP365>3.0.CO;2-J, 2000.

Kääb, A., Berthier, E., Nuth, C., Gardelle, J., and Arnaud, Y.: Contrasting patterns of early twenty-first-century glacier mass change in the Himalayas, Nature, 488, 495–498, https://doi.org/10.1038/nature11324, 2012.

Kääb, A., Winsvold, S.H., Altena, B., Nuth, C., Nagler, T., and Wuite, J.: Glacier remote sensing using Sentinel-2. Part I: Radiometric and geometric performance, and application to ice veloci-

FP 25 4 22 9:45 PM
Deleted: The

ty, Remote Sensing, 8(7), 598, https://doi.org/10.3390/rs8070598, 2016.

Kääb, A., Altena, B., and Mascaro, J.: Coseismic displacements of the 14 November 2016 Mw 7.8 Kaikoura, New Zealand, earthquake using the Planet optical cubesat constellation, Nat. Hazards Earth Syst. Sci., 17, 627–639, https://doi.org/10.5194/nhess-17-627-2017, 2017.

Kamb, B., Raymond, C.F., Harrison, W.D., Engelhardt, H., Echelmeyer, K.A., Humphrey, N., Brugman, M.M., amd Pfeffer, T.: Glacier surge mechanism: 1982–1983 surge of variegated glacier, Alaska. Science, 227(4686), 469-479, 1985.

King, O., Bhattacharya, A., and Bolch, T.: The presence and influence of glacier surging around the Geladandong ice caps, North East Tibetan Plateau, Advances in Climate Change Research, 12, 299–312, https://doi.org/10.1016/j.accre.2021.05.001, 2021.

Leclercq, P. W., Kääb, A., and Altena, B.: Brief communication: Detection of glacier surge activity using cloud computing of Sentinel-1 radar data, The Cryosphere, 15, 4901–4907, https://doi.org/10.5194/tc-15-4901-2021, 2021.

Leinss, S. and Bernhard, P.: TanDEM-X:Deriving InSAR Height Changes and Velocity Dynamics of Great Aletsch Glacier, IEEE J. Sel. Top. Appl. Earth Observations Remote Sensing, 14, 4798–4815, https://doi.org/10.1109/JSTARS.2021.3078084, 2021.

Lv, M., Guo, H., Lu, X., Liu, G., Yan, S., Ruan, Z., Ding, Y., and Quincey, D. J.: Characterizing the behaviour of surge- and non-surge-type glaciers in the Kingata Mountains, eastern Pamir, from 1999 to 2016, The Cryosphere, 13, 219–236, https://doi.org/10.5194/tc-13-219-2019, 2019.

Lv, M., Guo, H., Yan, J., Wu, K., Liu, G., Lu, X., Ruan, Z., and Yan, S.: Distinguishing Glaciers between Surging and Advancing by Remote Sensing: A Case Study in the Eastern Karakoram, Remote Sensing, 12, 2297, https://doi.org/10.3390/rs12142297, 2020.

Mayer, C., Fowler, A. C., Lambrecht, A., and Scharrer, K.: A surge of North Gasherbrum Glacier, Karakoram, China, 57, 904–916, https://doi.org/10.3189/002214311798043834, 2011.

Markus, T., Neumann, T., Martino, A., Abdalati, W., Brunt, K., Csatho, B., Farrell, S., Fricker, H., Gardner, A., Harding, D., Jasinski, M., Kwok, R., Magruder, L., Lubin, D., Luthcke, S., Morison, J., Nelson, R., Neuenschwander, A., Palm, S., Popescu, S., Shum, C.K., Schutz, B.E., Smith, B., Yang, Y., and Zwally, J.: The Ice, Cloud, and land Elevation Satellite-2 (ICESat-2): Science requirements, concept, and implementation. Remote Sensing of Environment, 190, 260-273, https://doi.org/10.1016/j.rse.2016.12.029, 2017.

Maussion, F., Scherer, D., Mölg, T., Collier, E., Curio, J., and Finkelnburg, R.: Precipitation Seasonality and Variability over the Tibetan Plateau as Resolved by the High Asia Reanalysis, 27, 1910–1927, https://doi.org/10.1175/JCLI-D-13-00282.1, 2014.

McNabb, R., Nuth, C., Kääb, A., and Girod, L.: Sensitivity of glacier volume change estimation to DEM void interpolation, The Cryosphere, 13, 895–910, https://doi.org/10.5194/tc-13-895-2019, 2019.

Millan, R., Mouginot, J., Rabatel, A., Jeong, S., Cusicanqui, D., Derkacheva, A., and Chekki, M.:

Mapping Surface Flow Velocity of Glaciers at Regional Scale Using a Multiple Sensors Approach, Remote Sensing, 11, 2498, https://doi.org/10.3390/rs11212498, 2019.

Murray, T., T. Strozzi, A. Luckman, H. Jiskoot, and P. Christakos, Is there a single surge mechanism? Contrasts in dynamics between glacier surges in Svalbard and other regions, J. Geophys. Res., 108(B5), 2237, https://doi.org/10.1029/2002JB001906, 2003.

Neumann, T. A., A. Brenner, D. Hancock, J. Robbins, J. Saba, K. Harbeck, A. Gibbons, J. Lee, S. B. Luthcke, T. Rebold, et al. 2021. *ATLAS/ICESat-2 L2A Global Geolocated Photon Data, Version 4*. Boulder, Colorado USA. NASA National Snow and Ice Data Center Distributed Active Archive Center. https://doi.org/10.5067/ATLAS/ATL03.004. [Last accessed 16 Octoctober 2021].

Neumann, T.: Technical Specs – ICESat-2 Ground Tracks, https://icesat-2.gsfc.nasa.gov/science/specs#:~:text=Over%20the%20polar%20areas%20and,measure%20more%20of%20Earth's%20forests, 2019 [last access: 15 April 2021].

NSIDC: ATL06 Known Issues (V03), https://nsidc.org/sites/nsidc.org/files/technical-references/ICESat2_ATL06_Known_issues_v003_Sept2020.pdf, 2020 [last access: 3 December 2020].

Nuth, C., Gilbert, A., Köhler, A., McNabb, R., Schellenberger, T., Sevestre, H., Weidle, C., Girod, L., Luckman, A., and Kääb, A.: Dynamic vulnerability revealed in the collapse of an Arctic tidewater glacier, Scientific Reports, 9, 5541, https://doi.org/ 10.1038/s41598-019-41117-0, 2019.

Obu, J., Westermann, S., Bartsch, A., Berdnikov, N., Christiansen, H. H., Dashtseren, A., Delaloye, R., Elberling, B., Etzelmüller, B., Kholodov, A., Khomutov, A., Kääb, A., Leibman, M. O., Lewkowicz, A. G., Panda, S. K., Romanovsky, V., Way, R. G., Westergaard-Nielsen, A., Wu, T., Yamkhin, J., and Zou, D.: Northern Hemisphere permafrost map based on TTOP modelling for 2000–2016 at 1 km^2 scale, Earth-Science Reviews, 193, 299–316, https://doi.org/10.1016/j.earscirev.2019.04.023, 2019.

Paul, F.: Revealing glacier flow and surge dynamics from animated satellite image sequences: examples from the Karakoram, The Cryosphere, 9, 2201–2214, https://doi.org/10.5194/tc-9-2201-2015, 2015.

Paul, F.: A 60-year chronology of glacier surges in the central Karakoram from the analysis of satellite image time-series, Geomorphology, 352, 106993, https://doi.org/10.1016/j.geomorph.2019.106993, 2020.

Paul, F., Bolch, T., Briggs, K., Kääb, A., McMillan, M., McNabb, R., Nagler, T., Nuth, C., Rastner, P., Strozzi, T., and Wuite, J.: Error sources and guidelines for quality assessment of glacier area, elevation change, and velocity products derived from satellite data in the Glaciers_cci project, Remote Sensing of Environment, 203, 256–275, https://doi.org/10.1016/j.rse.2017.08.038, 2017.

Paul, F., Strozzi, T., Schellenberger, T., and Kääb, A.: The 2015 Surge of Hispar Glacier in the

Karakoram, Remote Sensing, 9, 888, https://doi.org/10.3390/rs9090888, 2017.

Paul, F., Winsvold, S., Kääb, A., Nagler, T., and Schwaizer, G.: Glacier Remote Sensing Using Sentinel-2. Part II: Mapping Glacier Extents and Surface Facies, and Comparison to Landsat 8, Remote Sensing, 8, 575, https://doi.org/10.3390/rs8070575, 2016.

Pfeifer, N., Mandlburger, G., Otepka, J., and Karel, W.: OPALS – A framework for Airborne Laser Scanning data analysis, Computers, Environment and Urban Systems, 45, 125–136, https://doi.org/10.1016/j.compenvurbsys.2013.11.002, 2014.

Quincey, D. J., Glasser, N. F., Cook, S. J., and Luckman, A.: Heterogeneity in Karakoram glacier surges, J. Geophys. Res. Earth Surf., 120, 1288–1300, https://doi.org/10.1002/2015JF003515, 2015.

Rankl, M. and Braun, M.: Glacier elevation and mass changes over the central Karakoram region estimated from TanDEM-X and SRTM/X-SAR digital elevation models, Ann. Glaciol., 57, 273–281, https://doi.org/10.3189/2016AoG71A024, 2016.

Rankl, M., Kienholz, C., and Braun, M.: Glacier changes in the Karakoram region mapped by multimission satellite imagery, The Cryosphere, 8, 977–989, https://doi.org/10.5194/tc-8-977-2014, 2014.

Rashid, I., Majeed, U., Jan, A., and Glasser, N. F.: The January 2018 to September 2019 surge of Shisper Glacier, Pakistan, detected from remote sensing observations, Geomorphology, 351, 106957, https://doi.org/10.1016/j.geomorph.2019.106957, 2020.

Raymond, C. F.: How do glaciers surge? A review, J. Geophys. Res., 92, 9121, https ://doi.org/10.1029/JB092iB09p09121, 1987.

Round, V., Leinss, S., Huss, M., Haemmig, C., and Hajnsek, I.: Surge dynamics and lake outbursts of Kyagar Glacier, Karakoram, The Cryosphere, 11, 723–739, https://doi.org/10.5194/tc-11-723-2017, 2017.

Rupnik, E., Daakir, M., and Pierrot Deseilligny, M.: MicMac – a free, open-source solution for photogrammetry, Open geospatial data, softw. stand., 2, 14, https://doi.org/10.1186/s40965-017-0027-2, 2017.

Sakai, A.: Brief communication: Updated GAMDAM glacier inventory over high-mountain Asia, The Cryosphere, 13, 2043–2049, https://doi.org/10.5194/tc-13-2043-2019, 2019.

Sakai, A., Nuimura, T., Fujita, K., Takenaka, S., Nagai, H., and Lamsal, D.: Climate regime of Asian glaciers revealed by GAMDAM glacier inventory, The Cryosphere, 9, 865–880, https://doi.org/10.5194/tc-9-865-2015, 2015.

Sevestre, H. and Benn, D. I.: Climatic and geometric controls on the global distribution of surge-type glaciers: implications for a unifying model of surging, J. Glaciol., 61, 646–662, https://doi.org/10.3189/2015JoG14J136, 2015.

Sharp, M.: Surging glaciers: behaviour and mechanisms, Progress in Physical Geography: Earth and Environment, 12, 349–370, https://doi.org/10.1177/030913338801200302, 1988.

Shean, D.E., Alexandrov, O., Moratto, Z., Smith, B.E., Joughin, I.R., Porter, C.C. and Morin, P. J.:

An automated, open-source pipeline for mass production of digital elevation models (DEMs) from very high-resolution commercial stereo satellite imagery. ISPRS Journal of Photogrammetry and Remote Sensing, 116, 101–117, http://doi.org/10.1016/j.isprsjprs.2016.03.012, 2016.

Shean, D.: High Mountain Asia 8-meter DEM Mosaics Derived from Optical Imagery, Version 1, NASA NSIDC Distributed Active Archive Center, https://doi.org/10.5067/KXOVQ9L172S2, 2017, [last access: June 2021].

Shipton, E., Spender, M., and Auden, J. B.: The Shaksgam Expedition, 1937, The Geographical Journal, 91, 313, https://doi.org/10.2307/1788187, 1938.

Smith, B., Fricker, H. A., Gardner, A., Siegfried, M. R., Adusumilli, S., Csathó, B. M., Holschuh, N., Nilsson, J., Paolo, F.S, and the ICESat-2 Science Team: ATLAS/ICESat-2 L3A Land Ice Height, Version 3, NASA NSIDC Distributed Active Archive Center [dataset], https://doi.org/10.5067/ATLAS/ATL06.003, 2020, [last access: 3 December 2020].

Steiner, J. F., Kraaijenbrink, P. D. A., Jiduc, S. G., and Immerzeel, W. W.: Brief communication: The Khurdopin glacier surge revisited – extreme flow velocities and formation of a dammed lake in 2017, The Cryosphere, 12, 95–101, https://doi.org/10.5194/tc-12-95-2018, 2018.

Strozzi, T., Luckman, A., Murray, T., Wegmüller, U., and Werner, C. L.: Glacier motion estimation using SAR offset-tracking procedures, IEEE Trans. Geosci. Remote Sensing, 40, 2384–2391, https://doi.org/10.1109/TGRS.2002.805079, 2002.

Strozzi, T., Paul, F., Wiesmann, A., Schellenberger, T., and Kääb, A.: Circum-Arctic Changes in the Flow of Glaciers and Ice Caps from Satellite SAR Data between the 1990s and 2017, Remote Sensing, 9, 947, https://doi.org/10.3390/rs9090947, 2017.

USGS, Earth Resources Observation and Science (EROS) Center: USGS EROS Archive – Digital Elevation - Shuttle Radar Topography Mission (SRTM) 1 Arc-Second Global [dataset], https://doi.org/10.5066/F7PR7TFT, 2017, [last access: 2020].

Wang, X., Shangguan, D., Li, D., and Anjum, M. N.: Spatiotemporal Variability of Velocity and Influence of Glacier Thickness Using Landsat Imagery: Hunza River Basin, Karakoram Range, IEEE Access, 9, 72808–72819, https://doi.org/10.1109/ACCESS.2021.3078775, 2021.

Willis, M. J., Zheng, W., Durkin, W. J., Pritchard, M. E., Ramage, J. M., Dowdeswell, J. A., Benham, T. J., Bassford, R. P., Stearns, L. A., Glazovsky, A. F., Macheret, Y. Y., and Porter, C. C.: Massive destabilization of an Arctic ice cap, Earth and Planetary Science Letters, 502, 146–155, https://doi.org/10.1016/j.epsl.2018.08.049, 2018.

Wuite, J., Rott, H., Hetzenecker, M., Floricioiu, D., De Rydt, J., Gudmundsson, G. H., Nagler, T., and Kern, M.: Evolution of surface velocities and ice discharge of Larsen B outlet glaciers from 1995 to 2013, The Cryosphere, 9, 957–969, https://doi.org/10.5194/tc-9-957-2015, 2015.

Zhou, Y., Li, Z., and Li, J.: Slight glacier mass loss in the Karakoram region during the 1970s to 2000 revealed by KH-9 images and SRTM DEM, J. Glaciol., 63, 331–342, https://doi.org/10.1017/jog.2016.142, 2017.

FP 25 4 22 9:45 PM
Deleted: .

Tables

Table 1: Characteristics of the three investigated glaciers using outlines modified from the GAMDAM2 glacier inventory (Sakai et al. 2019) and digitized in this study. Elevations refer to the SRTM DEM. Values given for 'min/max' refer to the minimum and maximum extent of a glacier shortly before and after a surge, respectively.

	NN9	North Chongtar	South Chongtar
Size (min / max)	3.93 / 4.78 km^2	9.16 / 10.15 km^2	31.09 / 34.23 km^2
Size change (km^2 / percent)	+0.85 km^2 / +21.6%	+0.99 km^2 / +10.9%	+3.14 km^2 / +10.0%
Elevation (highest / mean)	6450 / 5620 m	6810 / 5860 m	7230 / 5920 m
Lowest elevation (min / max)	4430 / 5075 m	4440 / 5015 m	4545 / 4400 m
Length (min / max)	3.25 / 5.5 km	4.75 / 6.8 km	14.4 / 17.1 km
Changes (min. elev. / length)	645 / 2250 m	575 / 2050 m	145 / 2700 m
Slope / Aspect	31.5 / SE	28.8 / NW	25.1 / NW
Previous surge	1961-1971	1920s	1966-68
Surge repeat cycle	40-50 y	90 y?	54 y
This surge	2000-today	1965-today	2020-today
Characteristics	Compact dual-basin valley glacier with prominent medial moraine	Dual-basin valley glacier with one major tributary forming a prominent medial moraine	Long and flat single-basin valley glacier with three tributaries (one resulting in a short medial moraine)

Table 2: Overview of the DEMs used to determine elevation changes of the glaciers in the study region and the additional ICESat-2 dataset.

Nr.	Name (short)	Type	Reso-lution	Date	Source	Comments
1	SRTM 1	SAR	30 m	Feb. 2000	USGS, doi: 10.5066/f7pr7tft	C-band w/ penetration
2	HMA-DEM	OPT	8 m	Feb-Aug. 2015	NSIDC, doi: 10.5067/KXOVQ9L172S2	7 months composite
3	SPOT 2010	OPT	30 m	31 Oct 2010	Gardelle et al. 20013	SPOT 5 HRS
4	SPOT 2015	OPT	30 m	13 Oct 2015	Berthier & Brun 2019	SPOT 6
5	SPOT 2020	OPT	10 m	20 Oct 2020	Ordered from Airbus	SPOT 6
6	ASTER	OPT	30 m	2000-2019	Hugonnet et al. 2021	5y elevation changes
7	ICESat-2	LIDAR	0.7 m	3.12. 2018 – 5.11.2020	NSIDC, nsidc.org/data/icesat-2/data-sets	Version 4, 14 tracks, over glaciers only

Table 3: Calculated volume changes (in km^3) for six glaciers and different periods as obtained from the respective DEMs. Gray numbers in italics denote results that might be impacted by artefacts. See Fig. S5 for the location of the zones used to determine volume changes.

Nr.	Glacier	Period	Gain	Loss	Total
1	South Chongtar	2015-2020	0.3444	-0.1760	0.1684
2	North Chongtar	2000-2020	0.0466	-0.0365	0.0102
3	NN9	2000-2020	0.0356	*-0.0017*	0.0339
4	NN8	2000-2010	0.0175	-0.0167	0.0008
5	NN7	2000-2010	0.0146	-0.0304	-0.0158
6	Sarpo Laggo	2000-2020	*0.0024*	-0.4708	-0.4684

FP 25 4 22 9:45 PM
Deleted: *Grey umbers*

FP 25 4 22 9:45 PM
Deleted: Page Break

Figures

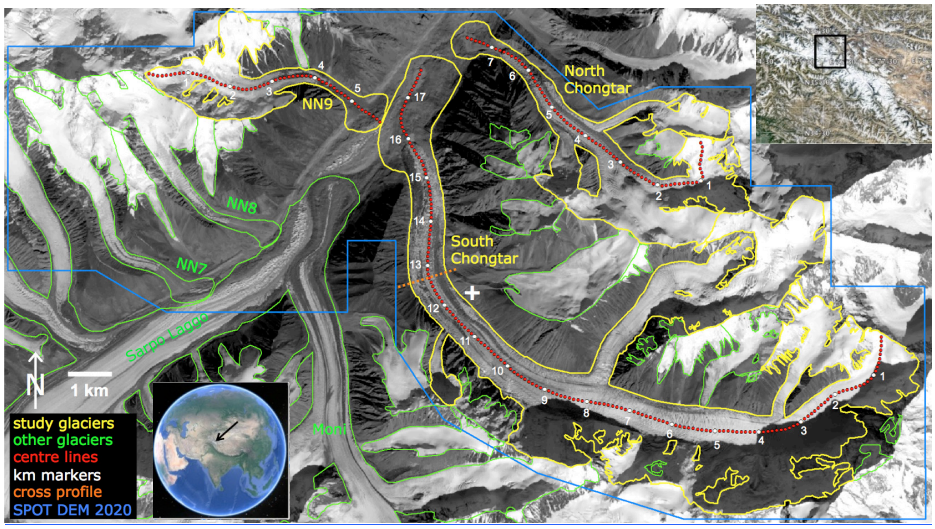

Fig. 1: Overview of the study region showing the location of the Karakoram Mountains (inset, lower left) and of the study region (inset upper right), outlines of the investigated glaciers (yellow), other glaciers (green), centre lines (red), km markers (white) cross-profile line (orange) and extent of the SPOT 2020 DEM perimeter (blue). The white + near the centre marks the coordinates 35.9°N and 76.34°E. The satellite image in the background is the Landsat 8 panchromatic band acquired on 21 Oct 2020. Credits: Landsat; earthexplorer.usgs.gov, the two insets are screenshots from Google Earth).

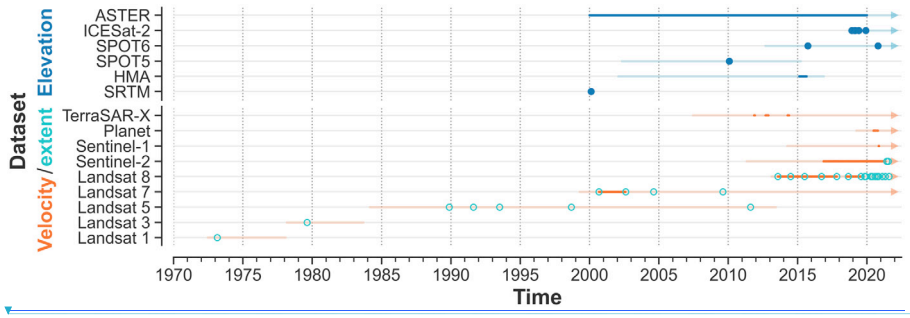

Figure 2. Timeline of the temporal coverage of the satellite sensors used (light line) and dates and time series selected for the analysis (lines or dots). Lines and dots in dark blue indicate the elevation change analysis, orange lines the velocity analysis, and green dots the glacier extents.

FP 25 4 22 9:45 PM
Deleted: .. ... [5]

FP 25 4 22 9:45 PM
Deleted: *from Landsat 8*

FP 25 4 22 9:45 PM
Deleted: *(*

FP 25 4 22 9:45 PM
Deleted: *data*

FP 25 4 22 9:45 PM
Deleted: *),*

FP 25 4 22 9:45 PM
Deleted: .

FP 25 4 22 9:45 PM
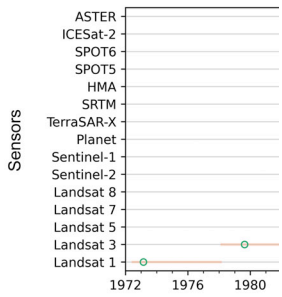

Deleted:

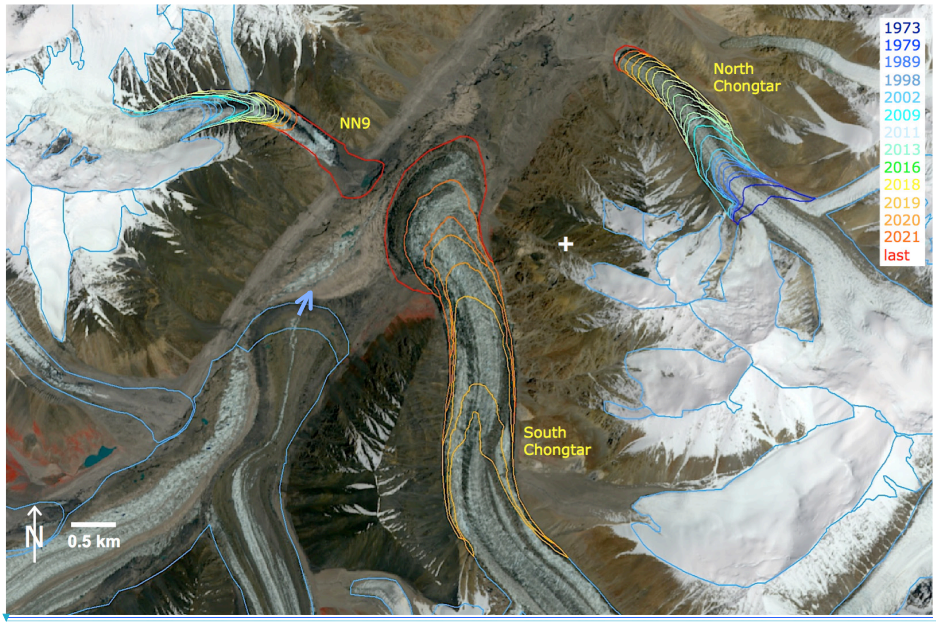

Fig. 3: Temporal evolution (colour-coded dates) of glacier extent for the three glaciers (NN9, North Chongtar, South Chongtar) investigated here. For comparison, the displacement of the terminal lobe of Moni Glacier from 2000 to 2020 is also shown (arrow). 'Last' is referring to 30 September 2021, the + sign near the centre marks the coordinates 35.93°N and 76.34°E. Background: Sentinel-2 image acquired on 16 July 2021 with bands 8/4/3 as RGB (Copernicus Sentinel data 2021).

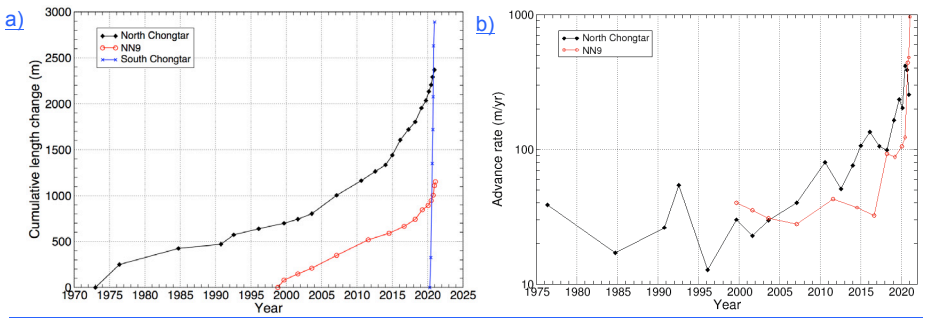

Fig. 4: Terminus changes for the investigated glaciers. a) Cumulative length changes (the retreat phase of South Chongtar before 2020 is not shown), b) advance rates.

FP 25 4 22 9:45 PM
Deleted: <sp>

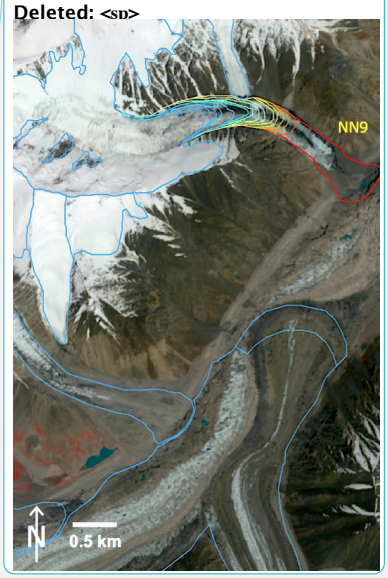

FP 25 4 22 9:45 PM
Deleted: .

FP 25 4 22 9:45 PM
Deleted: <sp><sp>
... [6]

FP 25 4 22 9:45 PM

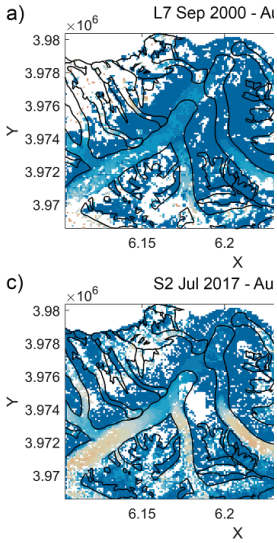

Deleted:

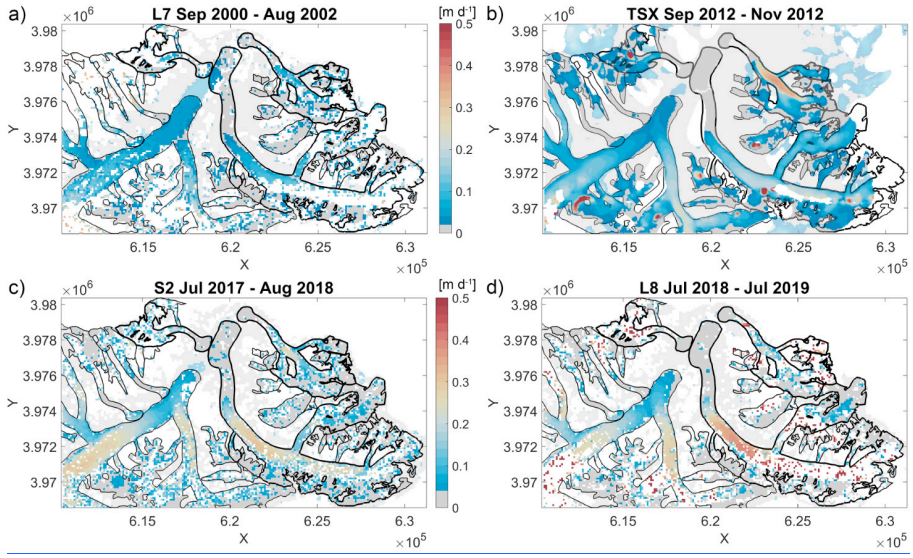

Fig. 5: Temporal evolution of 2D surface flow velocities for the three glaciers before 2020 derived from a) Landsat 7, b) TerraSAR-X, c) Sentinel-2, and d) Landsat 8. The dates of the compared images are given at the top of each panel. Grey values refer to velocities smaller than the uncertainty (see Table S2), i.e. <0.01 m d^{-1} for panels a) and b) and <0.02 m d^{-1} for c) and d).

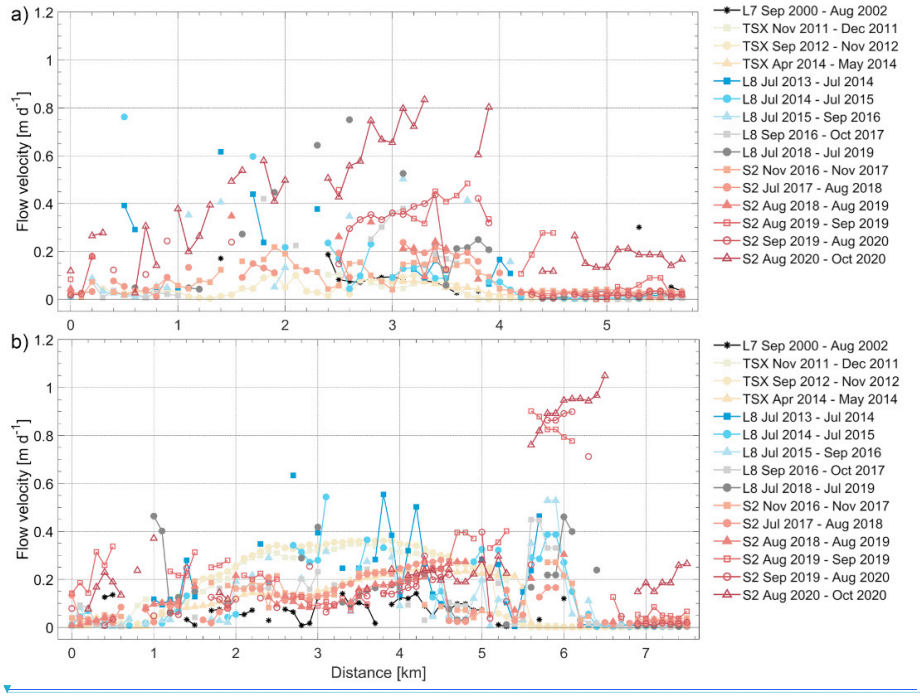

Fig. 6: Temporal evolution of 1D flow velocities along a centre-line starting at the highest point of each glacier for a) glacier NN9 and b) North Chongtar. Satellite names: L7/L8: Landsat 7/8, TSX:

FP 25 4 22 9:45 PM
Deleted: .. [7]

Terra-SAR-X, S2: Sentinel-2.

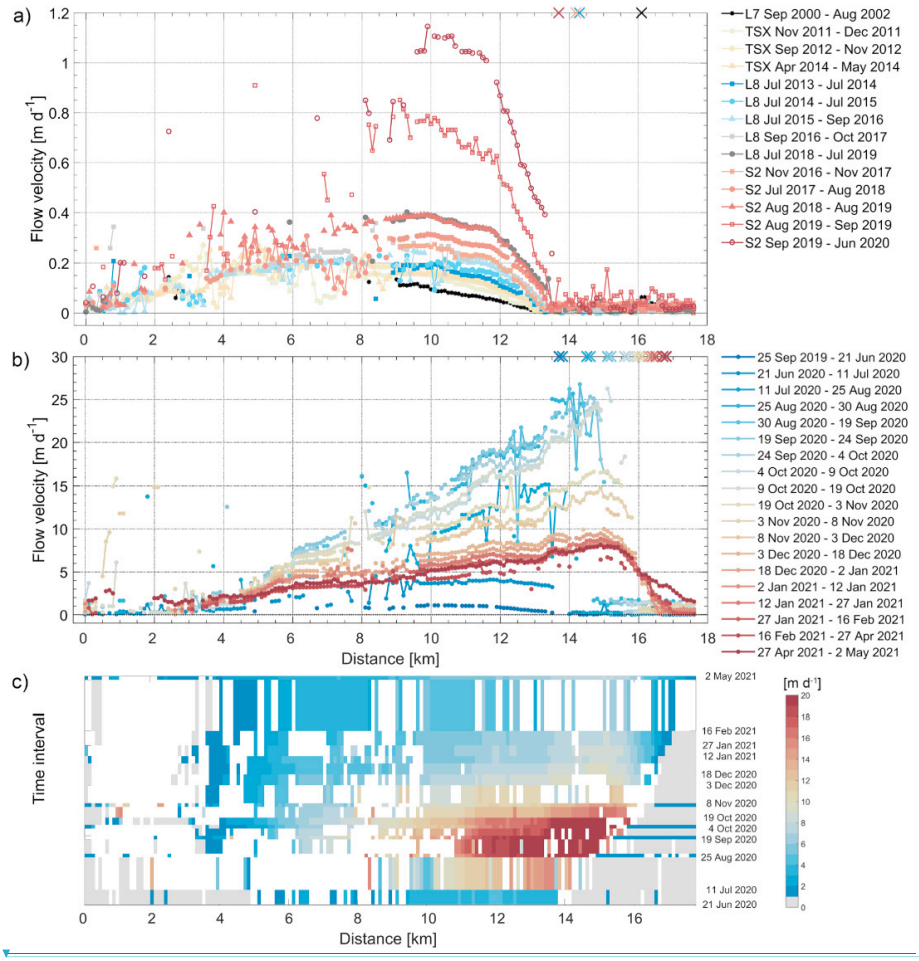

Fig. 7: Temporal evolution of flow velocities for South Chongtar Glacier from its highest point to its terminus, its location is indicated by an 'x' at the top of panels a) and b). a) Pre-surge values along the centre-line as derived from different satellites (names see Fig. 6). b) As a) but during the surge and derived from Sentinel-2 only, c) Hovmöller diagram of the surge phase. In this plot grey values are below 1 m d^{-1}, white indicates no data.

FP 25 4 22 9:45 PM
Deleted: .. [8]

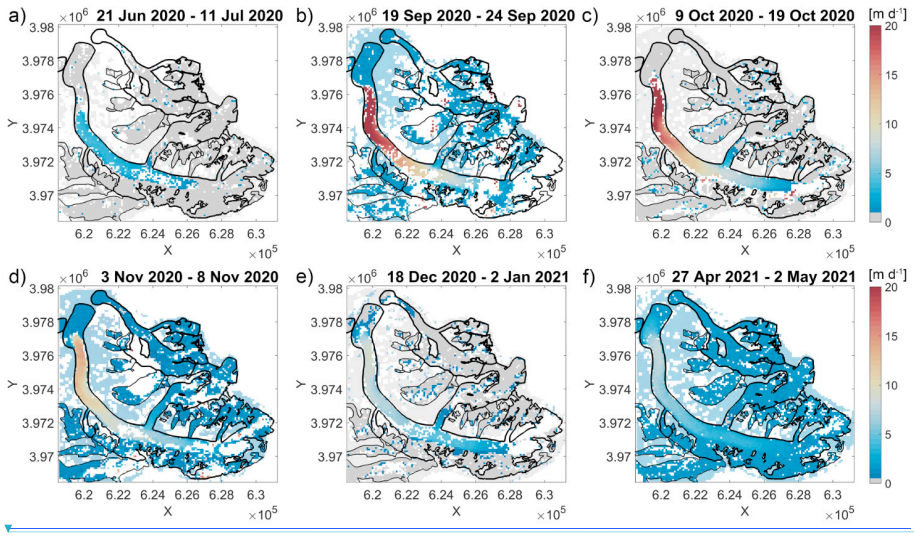

Fig. 8: Temporal evolution of 2D flow velocities for South Chongtar Glacier during its surge as derived from Sentinel-2. The dates of the respective Sentinel-2 pairs are given at the top of each panel. Grey values refer to velocities smaller than one standard deviation (see Table S2), i.e. <1 m d^{-1} for panels a) to c) and <0.5 m d^{-1} for d) to f).

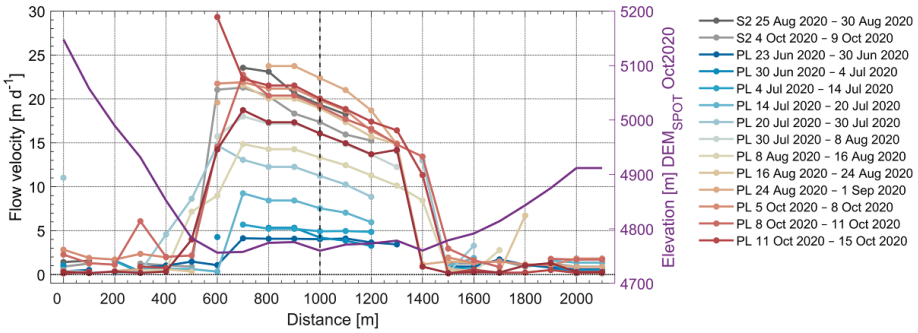

Fig. 9: South-west to north-east cross-profile surface flow velocities for South Chongtar Glacier derived from Planet and comparison with Sentinel-2. The vertical dash line indicates the location of the centerline. See Fig. 1 for location of the cross profile.

FP 25 4 22 9:45 PM
Deleted: <sp><sp><sp><sp><sp><sp>

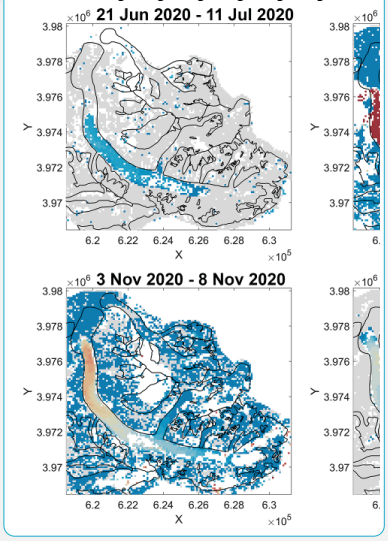

FP 25 4 22 9:45 PM
Deleted: *Cross*

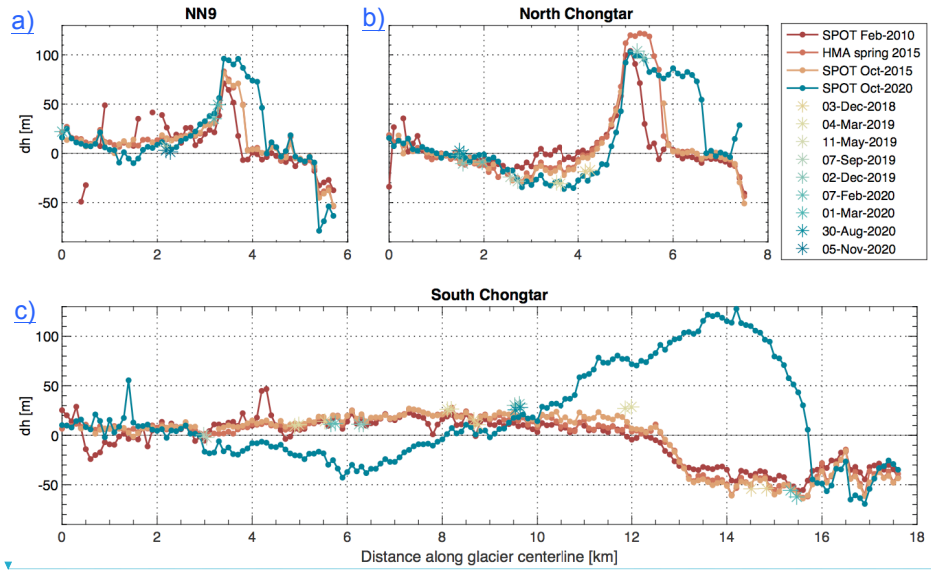

Fig. 10: Elevation differences along the glacier centerlines in respect to the SRTM DEM from 2000 for the three investigated glaciers, namely a) NN9, b) North Chongtar, and c) South Chongtar glaciers. The star (*) markers and dates in the legend correspond to ICESat-2 elevation differences with respect to the SRTM DEM. Note that due to the different track locations, only some of the dates shown in the legend are present in each panel.

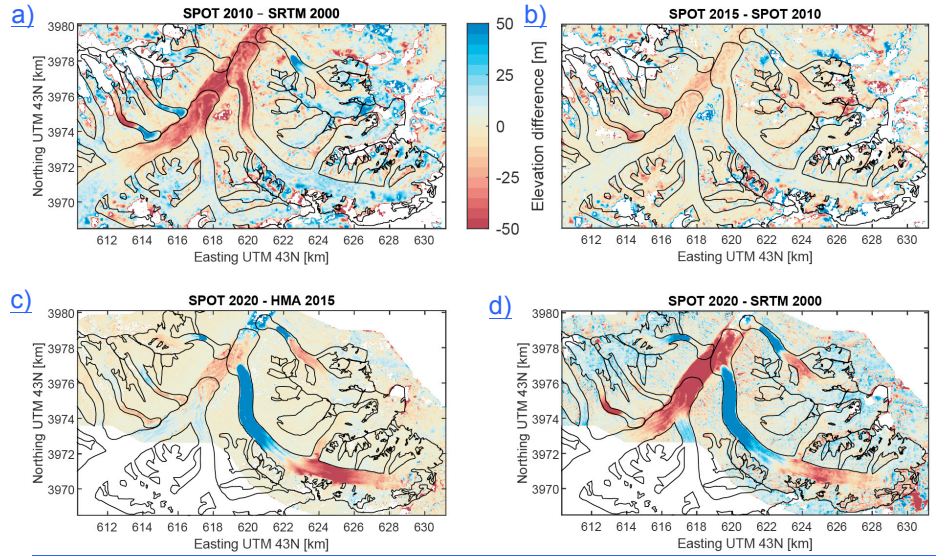

Fig. 11: 2D elevation difference maps over the study region. a) SPOT 2010 - SRTM 2000, b) SPOT 2015 - SPOT 2010, c) SPOT 2020 - HMA 2015, d) SPOT 2020 - SRTM 2000. A comparison between the SPOT 2015 and the HMA DEM from 2015 is shown in Fig. S13.

FP 25 4 22 9:45 PM
Deleted: <sp><sp><sp>

FP 25 4 22 9:45 PM
Deleted: in

FP 25 4 22 9:45 PM
Deleted: <sp><sp> ... [9]

FP 25 4 22 9:45 PM
Deleted: –

FP 25 4 22 9:45 PM
Deleted: –

FP 25 4 22 9:45 PM
Deleted: –

FP 25 4 22 9:45 PM
Deleted: –

Supplemental Material to:

Three different glacier surges at a spot: What satellites observe and what not

Frank Paul[1], Livia Piermattei[2], Desiree Treichler[2], Lin Gilbert[3], Andreas Kääb[2], Ludivine Libert[4], Thomas Nagler[4], Tazio Strozzi[5], Jan Wuite[4]

Supplemental Tables

Table S1: Overview of the Landsat (and two Sentinel-2) satellite images used for delineating glacier extents and determination of frontal advance rates. All scenes have been downloaded from earthexplorer.usgs.gov. The dataset is sorted by date, which is in the format DD MM YY without leading zero's. The scenes that have been selected for each glacier (might differ due to local clouds) are marked in the last three columns (x: yes, –: no). Glacier names: 'North Ch.': North Chongtar, 'South Ch.': South Chongtar.

Nr.	Satellite	Sensor	Path	Row	Date [YYYY/MM/DD]	NN9	North Ch.	South Ch.
1	Landsat 1	MSS	159	35	1973/02/24	–	x	–
2	Landsat 3	MSS	160	35	1979/08/19	–	x	–
3	Landsat 5	TM	148	35	1989/11/17	–	x	–
4	Landsat 5	TM	148	35	1991/08/19	–	x	–
5	Landsat 5	TM	148	35	1993/07/07	–	x	–
6	Landsat 5	TM	148	35	1998/09/07	x	x	–
7	Landsat 7	ETM+	148	35	2000/09/04	x	x	–
8	Landsat 7	ETM+	148	35	2002/08/09	x	x	–
9	Landsat 7	ETM+	148	35	2004/08/14	x	x	–
10	Landsat 7	ETM+	148	35	2009/08/12	x	x	–
11	Landsat 5	TM	148	35	2011/08/10	–	x	–
12	Landsat 8	OLI	148	35	2013/07/30	x	x	–
13	Landsat 8	OLI	148	35	2014/07/01	–	x	–
14	Landsat 8	OLI	148	35	2015/07/04	x	x	–
15	Landsat 8	OLI	148	35	2016/09/24	–	x	–
16	Landsat 8	OLI	148	35	2017/10/29	x	x	–
17	Landsat 8	OLI	148	35	2018/08/29	x	x	–
18	Landsat 8	OLI	148	35	2019/07/31	–	x	–
19	Landsat 8	OLI	148	35	2019/11/04	x	–	–
20	Landsat 8	OLI	148	35	2019/12/06	–	x	–
21	Landsat 8	OLI	148	35	2020/04/12	x	–	–
22	Landsat 8	OLI	148	35	2020/04/28	–	–	x
23	Landsat 8	OLI	148	35	2020/05/30	–	x	–
24	Landsat 8	OLI	148	35	2020/08/02	–	x	x
25	Landsat 8	OLI	148	35	2020/09/19	x	–	x
26	Landsat 8	OLI	148	35	2020/10/05	–	–	x
27	Landsat 8	OLI	148	35	2020/10/21	–	x	x
28	Landsat 8	OLI	148	35	2020/11/06	x	–	x
29	Landsat 8	OLI	148	35	2021/02/10	x	x	x
30	Landsat 8	OLI	148	35	2021/05/01	x	x	x
31	Sentinel-2	MSI	43	SFV	2021/06/06	x	–	x

FP 25 4 22 9:54 PM Deleted: The contrasting
FP 25 4 22 9:54 PM Deleted: of North
FP 25 4 22 9:54 PM Formatted ... [10]
FP 25 4 22 9:54 PM Formatted ... [11]
FP 25 4 22 9:54 PM Deleted: South Chongtar Glacier ... [12]
FP 25 4 22 9:54 PM Formatted ... [13]
FP 25 4 22 9:54 PM Formatted ... [14]
FP 25 4 22 9:54 PM Deleted: Sentine…entinel-2) satellit ... [15]
FP 25 4 22 9:54 PM Formatted Table ... [16]
FP 25 4 22 9:54 PM Deleted: N.-
FP 25 4 22 9:54 PM Deleted: S.-
FP 25 4 22 9:54 PM Deleted: 2 73
FP 25 4 22 9:54 PM Deleted: 8 79
FP 25 4 22 9:54 PM Deleted: 11 89
FP 25 4 22 9:54 PM Deleted: 8 91
FP 25 4 22 9:54 PM Deleted: 7 7 93
FP 25 4 22 9:54 PM Deleted: 7 9 98
FP 25 4 22 9:54 PM Deleted: 4 9 00
FP 25 4 22 9:54 PM Deleted: 9 8 02
FP 25 4 22 9:54 PM Deleted: 8 04
FP 25 4 22 9:54 PM Deleted: 8 09
FP 25 4 22 9:54 PM Deleted: 8 11
FP 25 4 22 9:54 PM Deleted: 7 13
FP 25 4 22 9:54 PM Deleted: 1 7 14
FP 25 4 22 9:54 PM Deleted: 4 7 15
FP 25 4 22 9:54 PM Deleted: 9 16
FP 25 4 22 9:54 PM Deleted: 10 17
FP 25 4 22 9:54 PM Deleted: 8 18
FP 25 4 22 9:54 PM Deleted: 7 19
FP 25 4 22 9:54 PM Deleted: 4
FP 25 4 22 9:54 PM Deleted: 19
FP 25 4 22 9:54 PM Formatted ... [17]
FP 25 4 22 9:54 PM ... [18]
FP 25 4 22 9:54 PM Formatted ... [19]
FP 25 4 22 9:54 PM
FP 25 4 22 9:54 PM Formatted ... [20]
FP 25 4 22 9:54 PM
FP 25 4 22 9:54 PM

32	Sentinel-2	MSI	43	SFV	2021/07/16	x	–	x
33	Landsat 8	OLI	148	35	2021/08/05	x	–	-

FP 25 4 22 9:54 PM
Deleted: 7 21

FP 25 4 22 9:54 PM
Deleted: 5 8 21

Table S2: Overview of the Landsat 7 (L7), Landsat 8 (L8), TerraSAR-X (TSX), Sentinel-2 (S2) and Planet (PL) satellite image pairs used for flow velocity analysis. The table is also listing for each scene pair the stable terrain velocities (mean, standard deviation 'Std' and median absolute deviation 'MAD') and the observed maximum flow velocities for the three glaciers NN9, North Chongtar 'N Ch.' and South Chongtar 'S Ch.' along the flow line.

Nr.	Sensor	Start date [YYYY/MM/DD]	End date [YYYY/MM/DD]	Time interval [day]	Velocity stable terrain [m d^{-1}]			Maximum velocity flowline [m d^{-1}]		
					Mean	Std	MAD	NN9	N Ch.	S Ch.
1	L7	2000/09/04	2002/08/04	699	0.01	0.03	0.01	0.30	0.14	0.14
2	L8	2013/07/30	2014/07/01	336	0.05	0.11	0.06	0.62	0.63	0.23
3	L8	2014/07/01	2015/07/04	368	0.04	0.14	0.06	0.76	0.54	0.23
4	L8	2015/07/04	2016/09/24	448	0.07	0.14	0.09	0.50	0.53	0.25
5	L8	2016/09/24	2017/10/29	400	0.03	0.07	0.04	0.42	0.45	0.36
6	L8	2018/07/12	2019/07/31	384	0.02	0.06	0.04	0.75	0.46	0.40
7	TSX	2011/11/12	2011/12/04	22	0.01	0.01	0.00	0.10	0.35	0.24
8	TSX	2012/09/09	2012/11/25	77	0.01	0.01	0.01	0.11	0.36	0.27
9	TSX	2014/04/10	2014/05/24	44	0.01	0.01	0.01	0.08	0.24	0.25
10	S2	2016/11/14	2017/11/04	355	0.04	0.02	0.01	0.22	0.27	0.30
11	S2	2017/07/27	2018/08/06	375	0.02	0.02	0.01	0.24	0.28	0.31
12	S2	2018/08/06	2019/08/06	365	0.03	0.03	0.01	0.35	0.30	0.40
13	S2	2019/08/06	2019/09/25	50	0.08	0.06	0.04	0.48	0.90	0.91
14	S2	2019/09/25	2020/08/25	335	0.02	0.03	0.01	0.44	0.90	-
15	S2	2020/08/25	2020/10/09	45	0.18	0.06	0.04	0.83	1.05	-
16	S2	2019/09/25	2020/06/21	270	0.09	0.19	0.12	-	-	1.15
17	S2	2020/06/21	2020/07/11	20	0.32	0.37	0.19	-	-	4.38
18	S2	2020/07/11	2020/08/25	45	0.30	1.12	0.29	-	-	16.62
19	S2	2020/08/25	2020/08/30	5	1.64	1.37	0.34	-	-	25.68
20	S2	2020/08/30	2020/09/19	20	0.23	1.27	0.22	-	-	26.77
21	S2	2020/09/19	2020/09/24	5	1.72	1.69	0.51	-	-	25.32
22	S2	2020/09/24	2020/10/04	10	0.67	1.65	0.48	-	-	24.52
23	S2	2020/10/04	2020/10/09	5	1.27	0.98	0.28	-	-	26.25
24	S2	2020/10/09	2020/10/19	10	0.42	0.59	0.11	-	-	24.05
25	S2	2020/10/19	2020/11/03	15	0.70	1.09	0.37	-	-	16.64
26	S2	2020/11/03	2020/11/08	5	1.17	0.94	0.38	-	-	14.85
27	S2	2020/11/08	2020/12/03	25	1.35	2.44	1.39	-	-	12.30
28	S2	2020/12/03	2020/12/18	15	0.23	0.31	0.14	-	-	10.00
29	S2	2020/12/18	2021/01/02	15	0.32	0.15	0.09	-	-	9.49
30	S2	2021/01/02	2021/01/12	10	0.68	0.37	0.17	-	-	8.54
31	S2	2021/01/12	2021/01/27	15	0.34	0.25	0.16	-	-	8.87
32	S2	2021/01/27	2021/02/16	20	0.30	0.59	0.24	-	-	8.13
33	S2	2021/02/16	2021/04/27	70	0.45	1.06	0.63	-	-	6.70
34	S2	2021/04/27	2021/05/02	8	1.63	0.30	0.24	-	-	8.17
35	PL	2020/06/23	2020/06/30	7	0.50	0.53	0.33	-	-	4.62
36	PL	2020/06/30	2020/07/04	4	1.19	1.05	0.70	-	-	5.51
37	PL	2020/07/04	2020/07/14	10	0.81	0.97	0.57	-	-	5.48
38	PL	2020/07/14	2020/07/20	6	2.73	2.72	2.30	-	-	8.43
39	PL	2020/07/20	2020/07/30	10	7.32	5.30	4.76	-	-	13.89
40	PL	2020/07/30	2020/08/08	9	0.71	1.59	0.58	-	-	17.79
41	PL	2020/08/08	2020/08/16	8	0.44	0.69	0.26	-	-	15.15
42	PL	2020/08/16	2020/08/24	8	0.62	0.69	0.31	-	-	22.20
43	PL	2020/08/24	2020/09/01	8	2.95	5.14	3.07	-	-	23.32
44	PL	2020/10/05	2020/10/08	3	2.01	1.81	1.42	-	-	30.81
45	PL	2020/10/08	2020/10/11	3	2.35	2.69	0.87	-	-	26.87
46	PL	2020/10/11	2020/10/15	4	1.32	3.86	1.42	-	-	27.99
47	PL	2020/10/15	2020/10/18	3	1.30	2.94	1.69	-	-	26.13

Deleted: *and… standard deviation* ... [24]
FP 25 4 22 9:54 PM
Deleted:
FP 25 4 22 9:54 PM
Deleted: (
FP 25 4 22 9:54 PM
Formatted ... [26]
FP 25 4 22 9:54 PM
Deleted: (
FP 25 4 22 9:54 PM
Deleted:
FP 25 4 22 9:54 PM
Formatted ... [28]
FP 25 4 22 9:54 PM
Deleted: Stable
FP 25 4 22 9:54 PM
Formatted ... [30]
FP 25 4 22 9:54 PM
Formatted ... [31]
FP 25 4 22 9:54 PM
Formatted Table ... [25]
FP 25 4 22 9:54 PM
Deleted: D)
FP 25 4 22 9:54 PM
Formatted ... [27]
FP 25 4 22 9:54 PM
Deleted: D)
FP 25 4 22 9:54 PM
Formatted ... [29]
FP 25 4 22 9:54 PM
Deleted: (days)
FP 25 4 22 9:54 PM
Deleted: (m d^{-1})
FP 25 4 22 9:54 PM
Deleted: ... [32]
FP 25 4 22 9:54 PM
Deleted: NN09 (m d^{-1})
FP 25 4 22 9:54 PM
Inserted Cells ... [33]
FP 25 4 22 9:54 PM
Deleted: (m d^{-1})
FP 25 4 22 9:54 PM
Deleted: … Ch. (m d^{-1}) ... [34]
FP 25 4 22 9:54 PM
Inserted Cells ... [35]
FP 25 4 22 9:54 PM
Deleted: 2107
FP 25 4 22 9:54 PM
Deleted: -
FP 25 4 22 9:54 PM
Inserted Cells ... [36]
FP 25 4 22 9:54 PM
Deleted: -
FP 25 4 22 9:54 PM
Deleted: -
FP 25 4 22 9:54 PM
Deleted: -
FP 25 4 22 9:54 PM
Deleted: -
FP 25 4 22 9:54 PM
Deleted: -
FP 25 4 22 9:54 PM
FP 25 4 22 9:54 PM
FP 25 4 22 9:54 PM
FP 25 4 22 9:54 PM
FP 25 4 22 9:54 PM
FP 25 4 22 9:54 PM
FP 25 4 22 9:54 PM

Table S3: Co-registration accuracy analysis over selected stable terrain areas (off-glacier, slope <40°). 'Std' is standard deviation, NMAD is the Normalized Median Absolute Difference. Regular font: accuracy measures from differences with regard to the HMA DEM (the co-registration base), italic font: statistics for other computed DEM differences.

Datasets	Elevation difference [m]					
	Mean	Std.	Median	NMAD	Minimum	Maximum
HMA DEM 2015 – SPOT 2010 (30 m)	1.32	9.87	1.03	6.53	-104.01	379.34
HMA DEM 2015 – SPOT 2015 (30 m)	0.51	13.24	-0.12	1.62	-51.09	423.18
HMA DEM 2015 – SRTM 2000 (30 m)	0.63	9.37	1.02	5.97	-113.01	154.48
SPOT 2020 – HMA DEM 2015 (5 m)	1.28	3.07	1.08	2.32	-176.69	61.57
SPOT 2010 – SRTM 2000 (30 m)	*-0.58*	*11.45*	*-0.31*	*8.68*	*-365.42*	*143.25*
SPOT 2015 – SPOT 2010 (30 m)	*0.78*	*15.85*	*1.22*	*6.77*	*-424.44*	*118.07*
SPOT 2020 – SRTM 2000 (30 m)	*2.37*	*8.80*	*2.54*	*6.37*	*-103.09*	*59.33*
SPOT 2020 – SRTM 2000 (5 m)	*3.10*	*11.05*	*3.47*	*9.43*	*-257.99*	*101.48*

Formatted ... [37]
FP 25 4 22 9:54 PM
Deleted: 'Std.' is standard deviation
FP 25 4 22 9:54 PM
Deleted: Datasets
FP 25 4 22 9:54 PM
Merged Cells ... [38]
FP 25 4 22 9:54 PM
Deleted: .
FP 25 4 22 9:54 PM
Inserted Cells ... [39]
FP 25 4 22 9:54 PM
Deleted: 3234
FP 25 4 22 9:54 PM
Deleted: 8660
FP 25 4 22 9:54 PM
Deleted: 0303
FP 25 4 22 9:54 PM
Deleted: 3369
FP 25 4 22 9:54 PM
Deleted: 5066
FP 25 4 22 9:54 PM
Deleted: 2438
FP 25 4 22 9:54 PM
Deleted: 1199
FP 25 4 22 9:54 PM
Deleted: 1772
FP 25 4 22 9:54 PM
Deleted: 6316
FP 25 4 22 9:54 PM
Deleted: 3655
FP 25 4 22 9:54 PM
Deleted: 0229
FP 25 4 22 9:54 PM
Deleted: 4829
FP 25 4 22 9:54 PM
Deleted: 2817
FP 25 4 22 9:54 PM
Deleted: 0735
FP 25 4 22 9:54 PM
Deleted: 0840
FP 25 4 22 9:54 PM
Deleted: 5708
FP 25 4 22 9:54 PM
Deleted: *5831*
FP 25 4 22 9:54 PM
Deleted: *4501*
FP 25 4 22 9:54 PM
Deleted: *3081*
FP 25 4 22 9:54 PM
Deleted: *2505*
FP 25 4 22 9:54 PM
Deleted: *7842*
FP 25 4 22 9:54 PM
Deleted: *8529*
FP 25 4 22 9:54 PM
Deleted: *2217*
FP 25 4 22 9:54 PM
Deleted: *0737*
FP 25 4 22 9:54 PM
Deleted: *3728*
FP 25 4 22 9:54 PM
FP 25 4 22 9:54 PM
FP 25 4 22 9:54 PM
FP 25 4 22 9:54 PM
FP 25 4 22 9:54 PM
FP 25 4 22 9:54 PM
FP 25 4 22 9:54 PM

Supplemental Figures

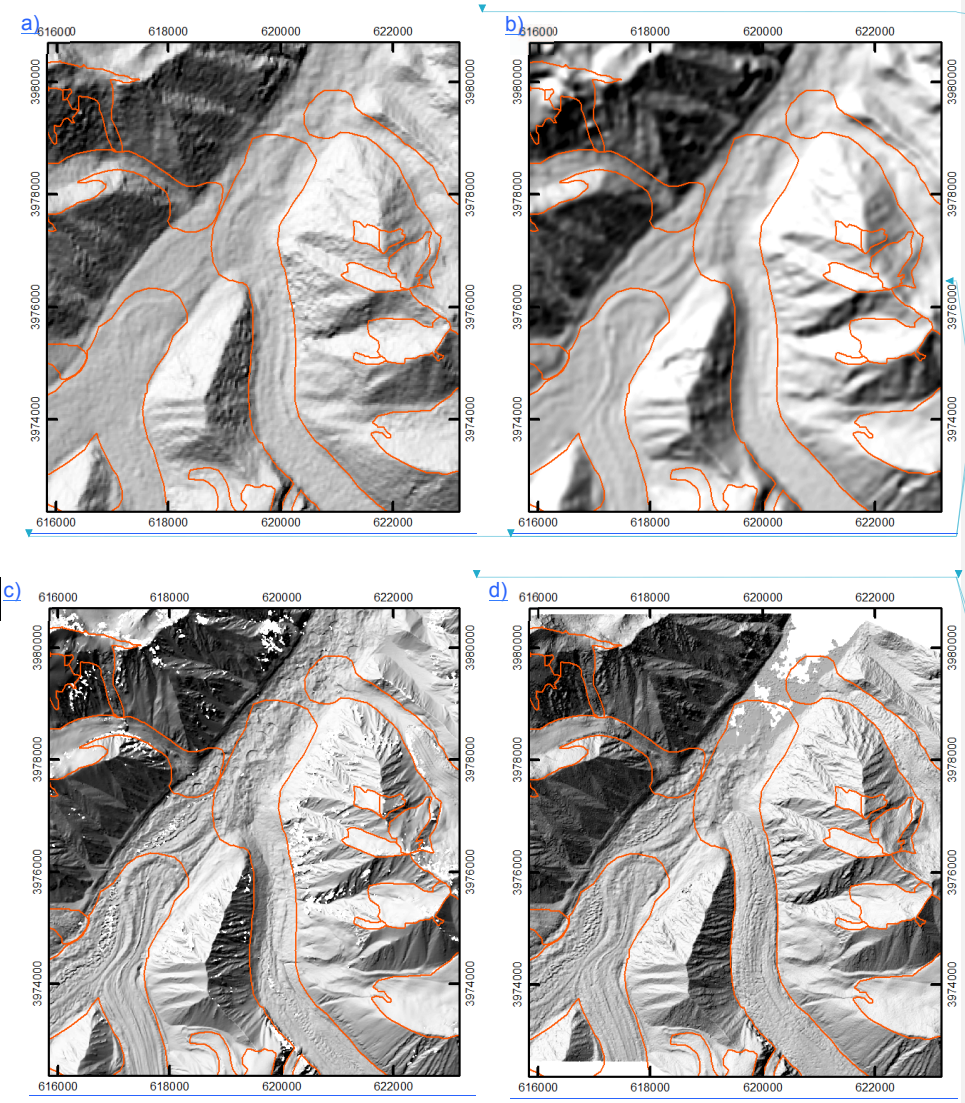

Fig. S1: Comparison of hillshades of the DEMs used. a) SRTM DEM (30 m, Feb. 2000), b) SPOT DEM (40 m, 2010), c) HMA DEM (8 m, 16.07.2017), d) SPOT Pleiades (3 m, 20.10.2020). The SPOT 2015 DEM (not shown) has the same visual/accuracy properties as the SPOT 2010 DEM shown here. Coordinates: UTM 34N [m].

FP 25 4 22 9:54 PM
Deleted: <sp><sp>

FP 25 4 22 9:54 PM
Deleted: <sp> ... [41]

FP 25 4 22 9:54 PM

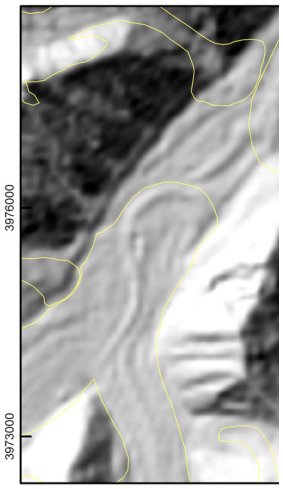

Deleted:

FP 25 4 22 9:54 PM
Formatted Table

FP 25 4 22 9:54 PM
Deleted: <sp> ... [42]

FP 25 4 22 9:54 PM

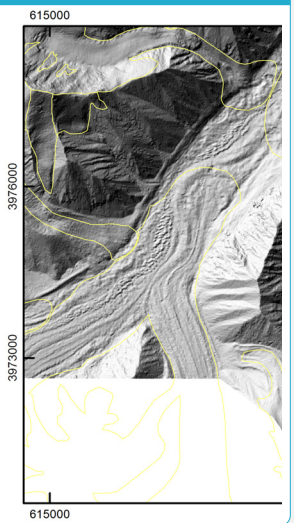

Deleted:

FP 25 4 22 9:54 PM
Formatted: English (US)

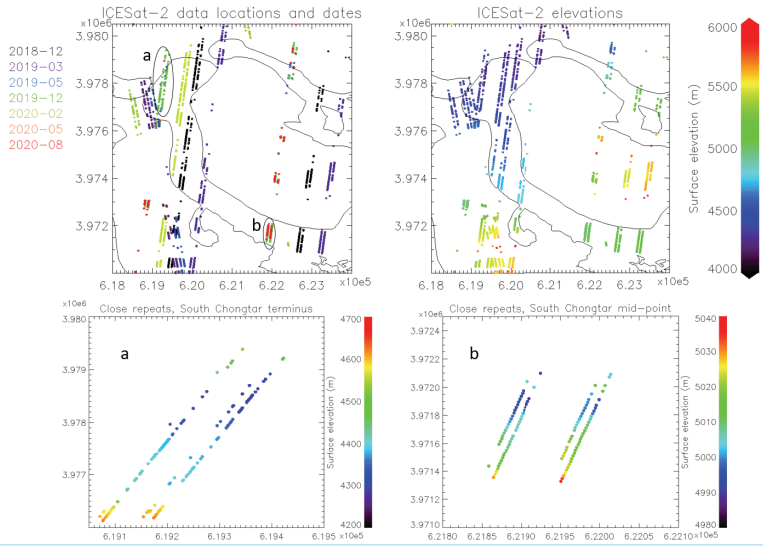

Fig. S2: ICESat-2 ATL06 data locations, coloured by date (in years and months, above left) and elevation (in m, above right). Elevations for closely repeating tracks in the two ringed areas a and b are shown below on a larger scale, demonstrating their separation. Coordinates: UTM 34N [m].

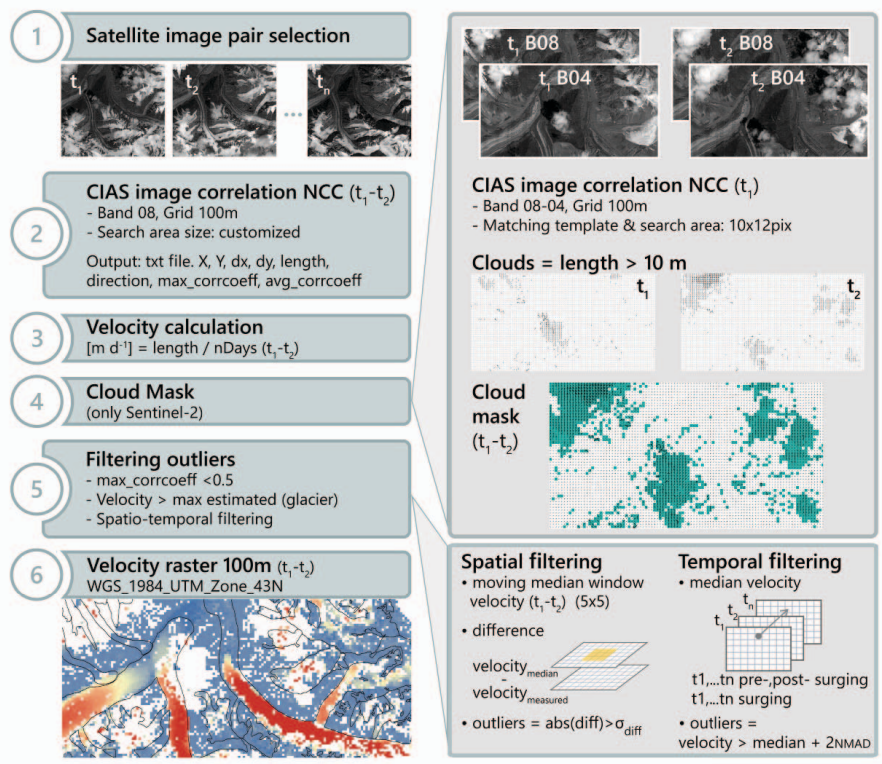

Fig S3: Workflow to calculate glacier surface displacement with CIAS.

FP 25 4 22 9:54 PM
Deleted: .

FP 25 4 22 9:54 PM
Formatted: Centered

FP 25 4 22 9:54 PM
Formatted: Centered

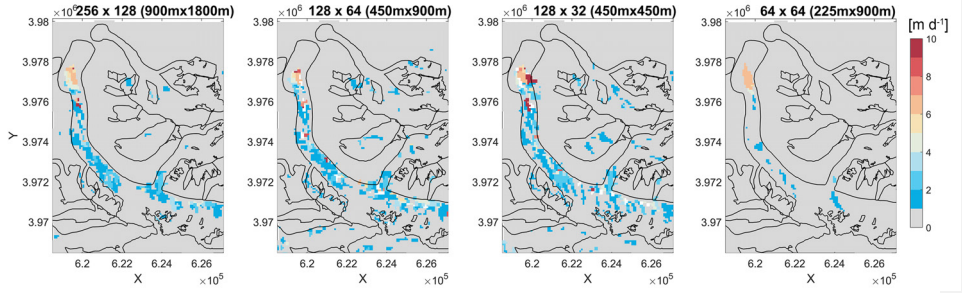

Fig. S4: Sentinel-1 image template size tests (extensions are given on top of each panel). Coordinates: UTM 34N [m].

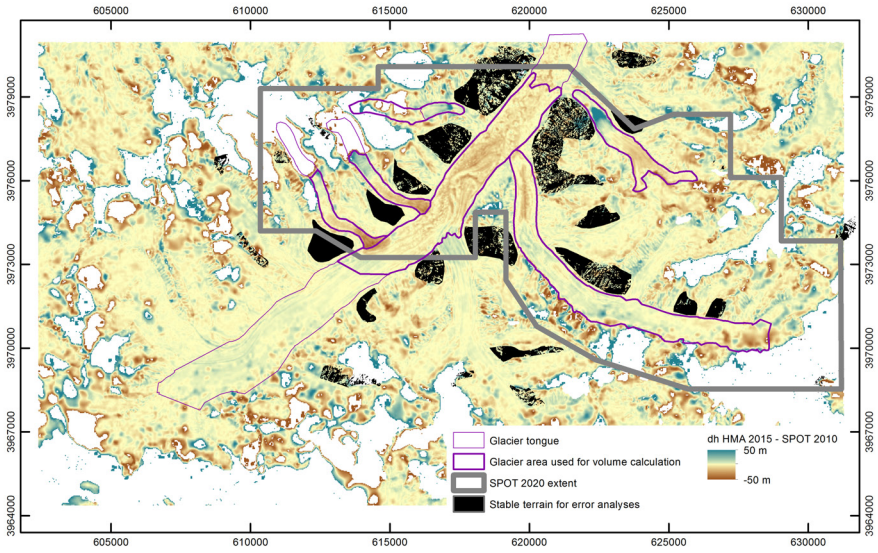

Fig. S5: Stable areas, error assessment and volume changes: Several patches of stable terrain with slope < 40° (black regions) were used to co-register the DEMs and to estimate uncertainties for both elevation changes and velocity analyses. Surge volume changes were computed for the purple glacier tongue parts, specifically adjusted from the maximum glacier outlines shown in Figs. 1 and 3, to capture the area of maximum volume changes for each glacier separately, and to remove no data, or accumulation areas biased by artifacts. In the background: elevation differences between HMA DEM 2015 – SPOT 2010, which are very similar to the SPOT 2015 – SPOT 2010 in Fig. 11b. Coordinates: UTM 34N [m].

FP 25 4 22 9:54 PM
Formatted: Centered

FP 25 4 22 9:54 PM
Deleted: */biased*

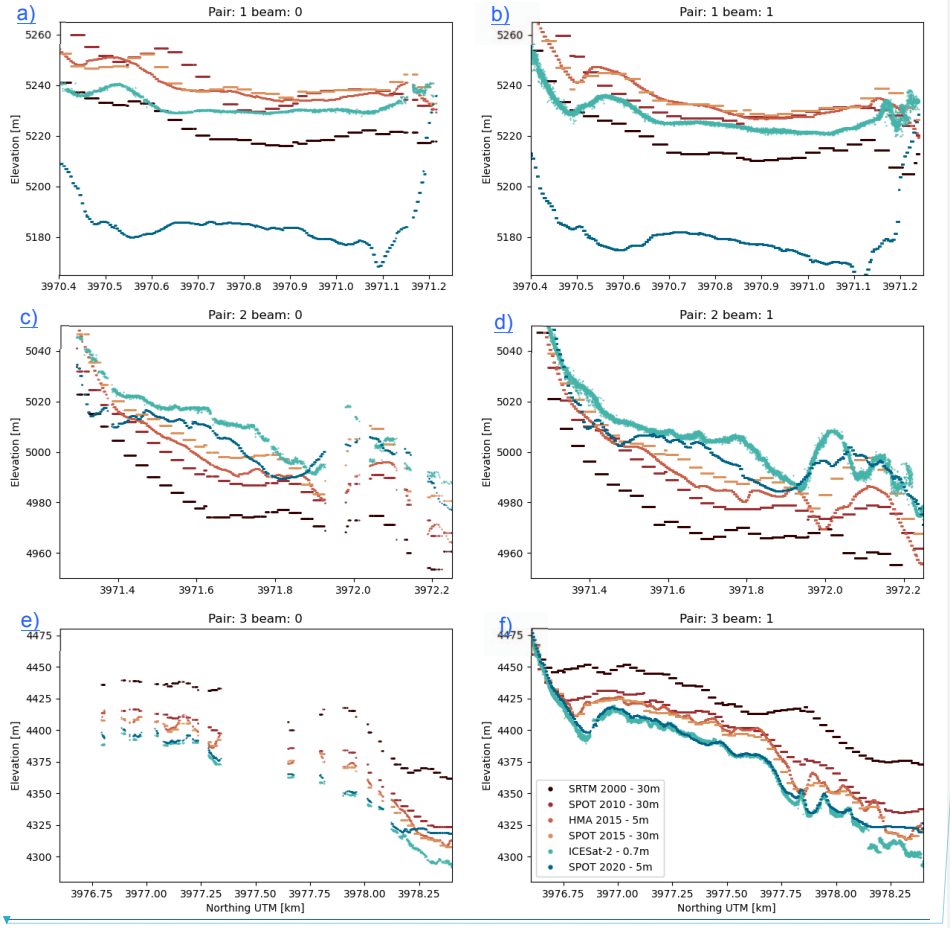

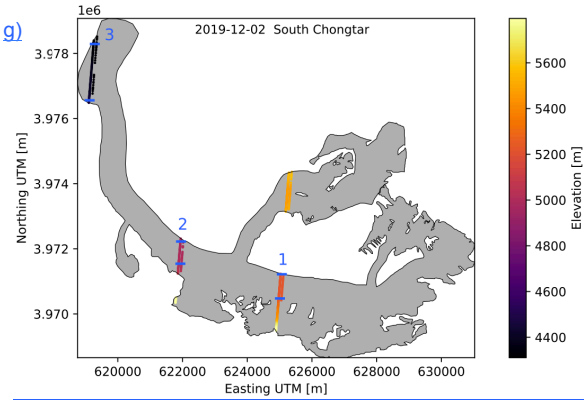

Fig. S6: a) to f) Elevation profiles of one ICESat-2 overpass over the tongue of South Chongtar glacier on 2 December 2019. Filtered ATL03 photon elevations are shown in blue, corresponding SRTM DEM elevations in black. The profiles are numbered from East to West (see map in panel g), i.e. profile 1 is highest up on the glacier. The left panels show the weak laser beam, the right panels the strong laser beam with ca. four times as many photons per pulse shot. g) Locations of

FP 25 4 22 9:54 PM
Deleted: *<sp>*

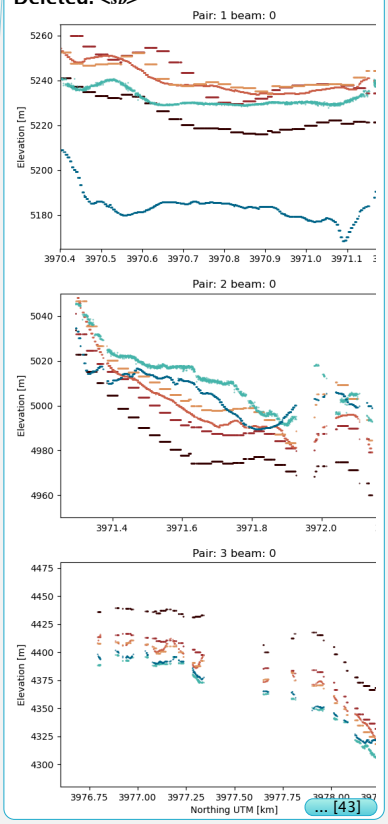

FP 25 4 22 9:54 PM
Deleted: *February*

FP 25 4 22 9:54 PM
Deleted: *b*

FP 25 4 22 9:54 PM
Deleted: *b*

the six elevation profiles on South Chongtar glacier in a) to f). The blue markers and numbers indicate which part of the glacier tongue is shown in a) to f), and the profile number. The easternmost beam of each pair is the weak beam. Coordinates: UTM 34N.

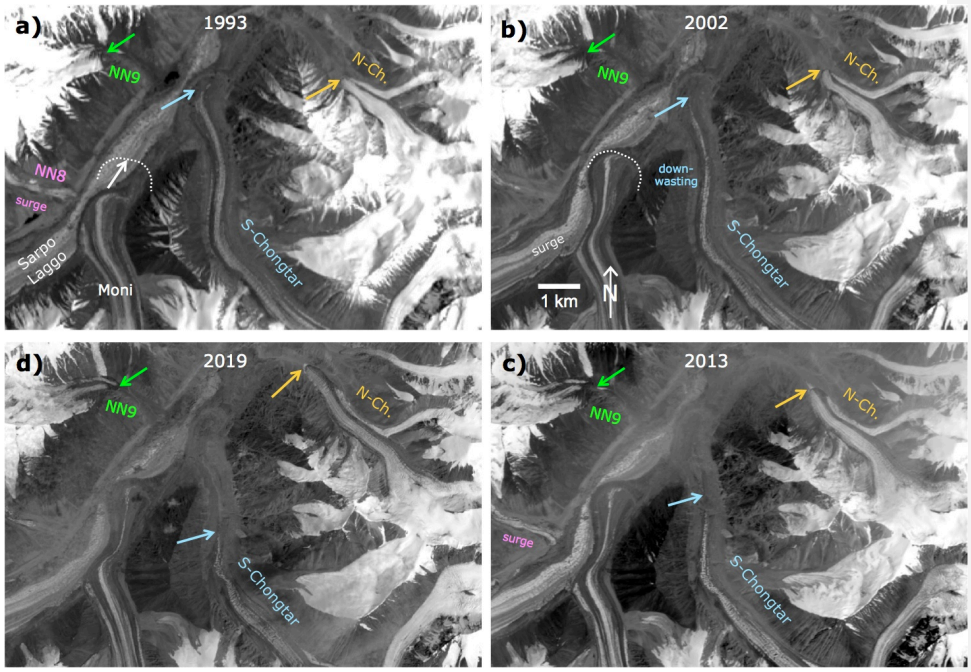

Fig. S7: Time series of glacier extents before the surge of South Chongtar (S. Chongtar) as seen with (clockwise) a) Landsat 5 in 1993, b) Landsat 7 in 2002, c) Landsat 8 in 2013 and d) Landsat 8 in 2019. The arrows at each glacier point to the terminus position at the time of image acquisition. The two surges of the neighbouring glacier NN8 are also indicated, N-Ch. is North Chongtar. The advance of North Chongtar and the downwasting of South Chongtar can be well followed. The advance of NN9 is limited. (Image source: earthexplorer.usgs.gov).

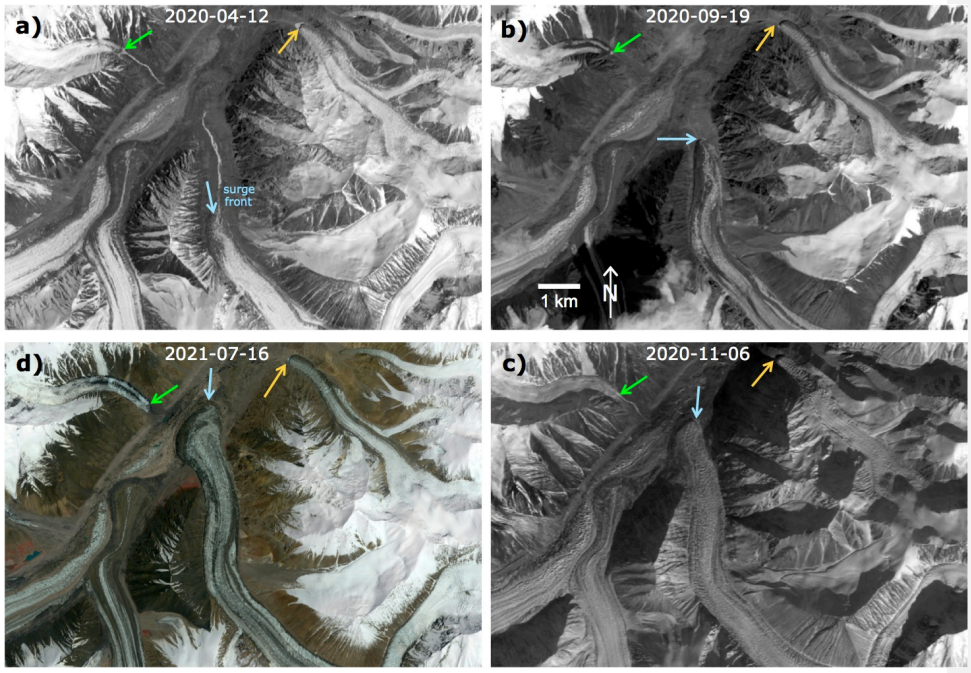

Fig. S8: Time series of glacier extents during the surge of South Chongtar (S. Chongtar) as seen with the Landsat 8 panchromatic band (clockwise) in a) 12 April 2020, b) 19 September 2020, c) 6 November 2020 and d) with Sentinel-2 on 17 June 2021. The arrows at each glacier point to the terminus position at the time of image acquisition. (Image sources a) to c): earthexplorer.usgs.gov, d): Copernicus Sentinel data 2021).

FP 25 4 22 9:54 PM
Deleted: :

FP 25 4 22 9:54 PM
Deleted: *(Landsat 8),*

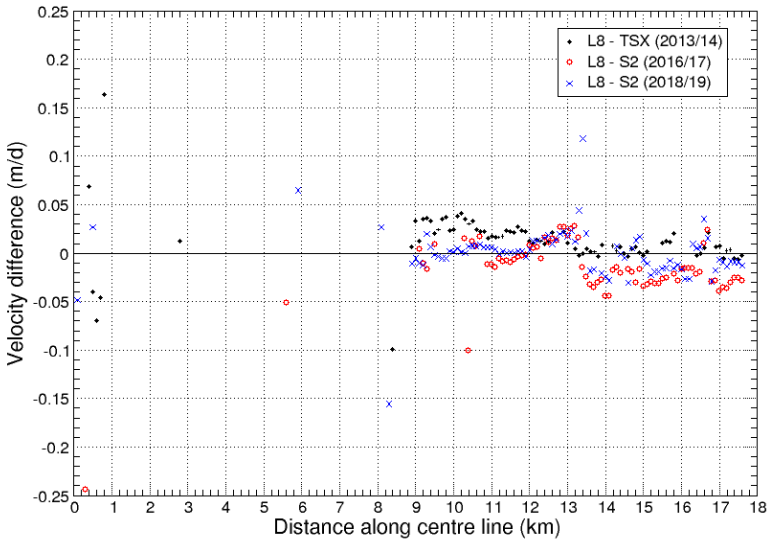

Fig. S9: Differences in flow velocities along the centre line of South Chongtar Glacier derived from Landsat 8 and TSX as well as Landsat 8 and Sentinel-2 image pairs from three periods.

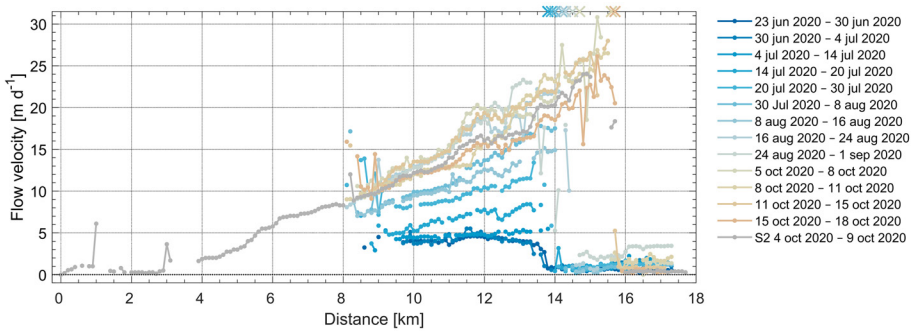

Fig. S10: Flow velocity time series derived from Planet (surge phase South Chongtar). The 'x' letters at the top mark the terminus position.

FP 25 4 22 9:54 PM
Moved (insertion) [7]

FP 25 4 22 9:54 PM
Moved up [7]: *Fig.*

FP 25 4 22 9:54 PM
Moved (insertion) [8]

FP 25 4 22 9:54 PM

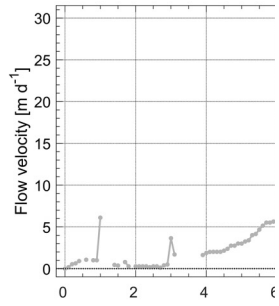

Deleted:

FP 25 4 22 9:54 PM
Deleted: *S9*

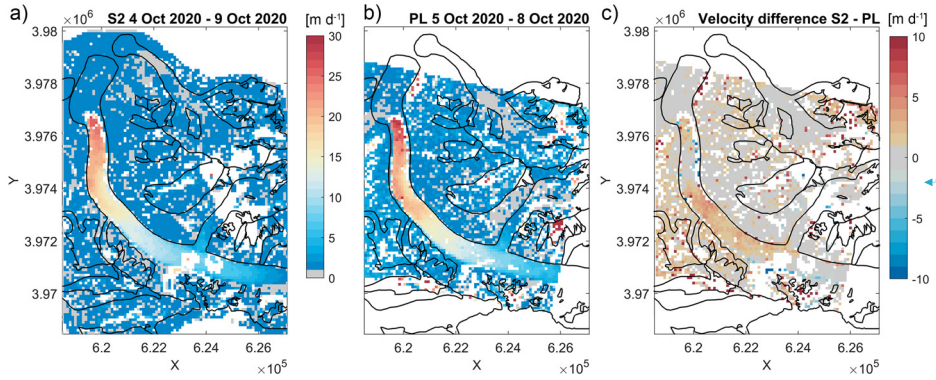

Fig. S11: 2D flow velocity maps. Comparison between a) Sentinel-2, b) Planet, and c) their difference. Coordinates: UTM 34N [m].

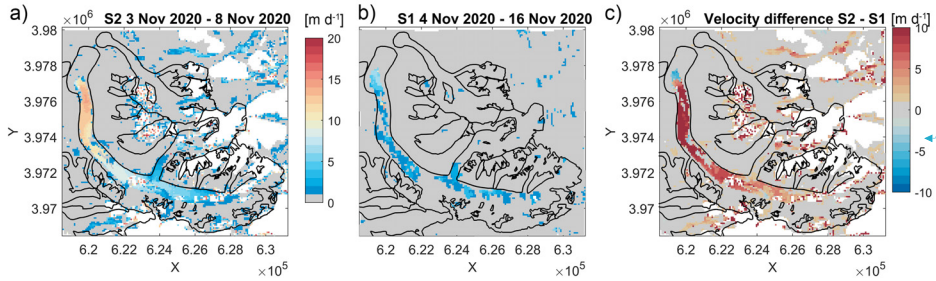

Fig. S12: Comparison of 2D flow velocity maps derived from a) Sentinel-2 and b) Sentinel-1. Panel c) shows their difference. Coordinates: UTM 34N [m].

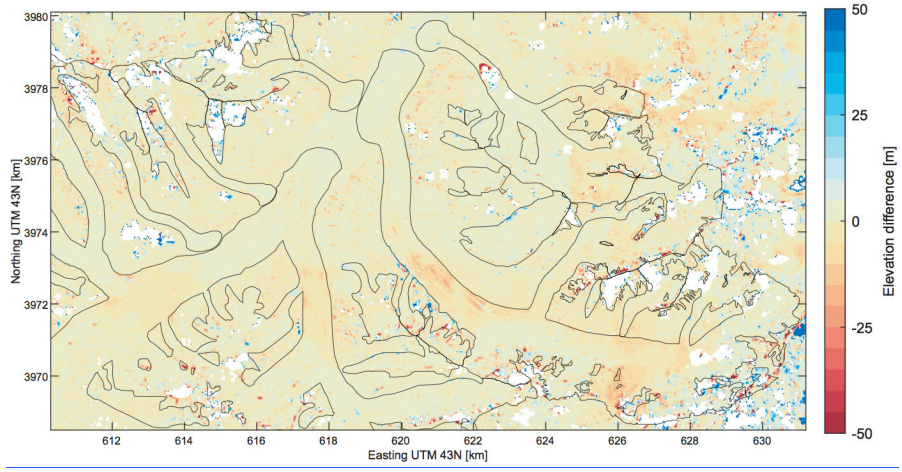

Fig. S13: DEM comparison subtracting the SPOT2015 from the HMA2015 DEM. The SPOT DEM

FP 25 4 22 9:54 PM
Formatted: Centered

FP 25 4 22 9:54 PM
Deleted: *S10*

FP 25 4 22 9:54 PM
Formatted: Centered

FP 25 4 22 9:54 PM
Deleted: *S11:*

FP 25 4 22 9:54 PM
Deleted: *. Comparison between*

FP 25 4 22 9:54 PM
Deleted: *,*

FP 25 4 22 9:54 PM
Deleted: *, and*

FP 25 4 22 9:54 PM
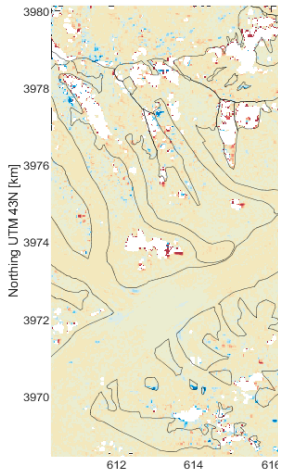

Deleted:

was generated from a single image pair from October 2015, while the HMA DEM mosaic is a composite of in total 15 DEM stripes acquired predominantly in 2015 (eight scenes from Feb to Aug, two scenes in October). These are complemented with four scenes from 2009 to 2011 and one from 2009, all covering only very small parts of the glaciers. The coloured dots are related to artefacts in steep terrain except the blue half circle (upper centre) marking the advance of North Chongtar.

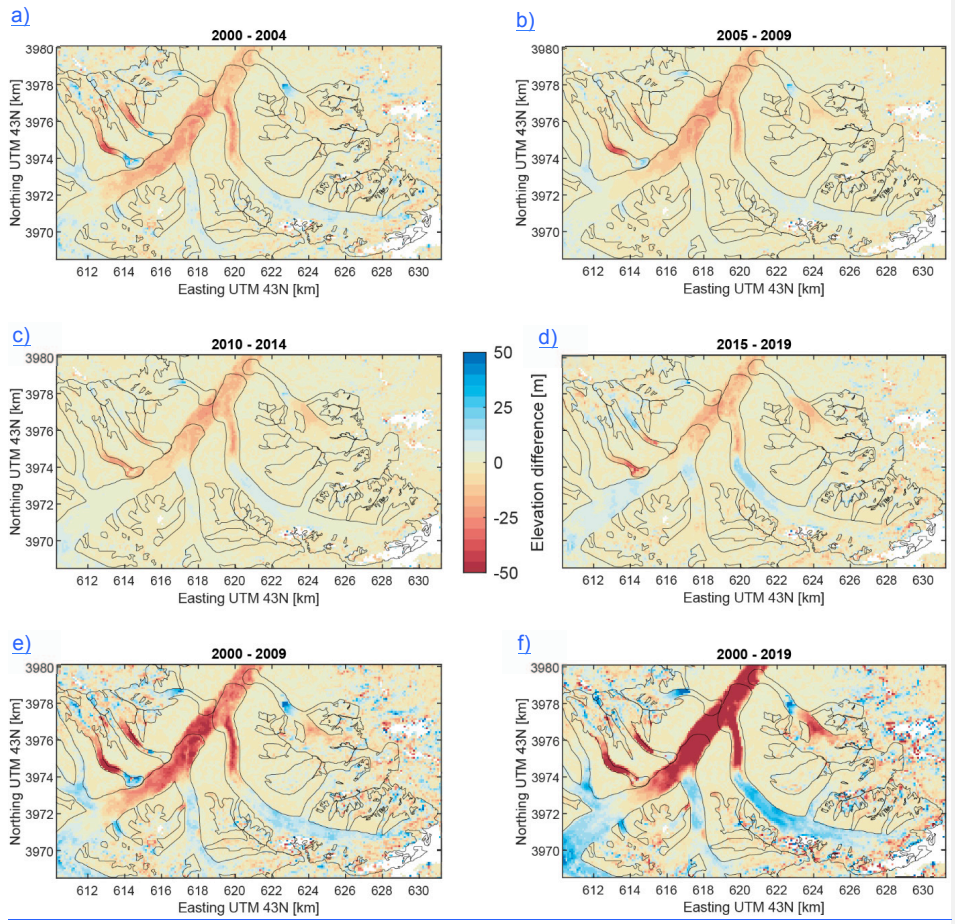

Fig. S14: DEM differences over four periods from Hugonnet et al. (2021). All years in this study refer to the full calendar year, i.e. the time intervals covered are five years for each of the panels a) to d), 10 years for e) and 20 years for f). The periods are: a) 2000-2004, b) 2005-2009, c) 2010-2014, d) 2015-2019, e) 2000-2009, f) 2000-2019.

FP 25 4 22 9:54 PM
Moved up [8]: *Fig.*

FP 25 4 22 9:54 PM
Deleted: *S12: DEM comparison subtracting the SPOT 2015 from the HMA 2015 DEM. It is likely that the negative values (red colours) to the east of 625 000 m E are a tiling artefact in the HMA DEM, caused by elevation source data from 2010 which contributes to the composite in this part of the DEM.* ... [44]

FP 25 4 22 9:54 PM
Deleted: *S13*

FP 25 4 22 9:54 PM
Deleted: *2021.*

FP 25 4 22 9:54 PM
Deleted: *2010-*

FP 25 4 22 9:54 PM
Deleted: *2020-*

Supplemental animation

FP 25 4 22 9:54 PM
Deleted: animations

Time series from Sentinel-1

Radar satellites can 'see' through clouds and Sentinel-1 offers frequent and systematic coverage in areas prone to monsoon clouds as the Himalayas. Despite radar speckle and 74 m x 56 m spatial resolution of 20x4 multi-looked products, the rapid advance of Chongtar glacier since July 2020 can be clearly observed in Sentinel-1 backscattering intensity images (Figure SA). Changes in backscattering intensity at the glacier surface are mostly due to a change in the physical properties of the ice, e.g. liquid water resulting from melting reduces intensity considerably. The animation of 12-days Sentinel-1 backscattering intensity images shows the sudden advance of South Chongtar glacier in Summer 2020. The file is named 'chongtar_surge_anim.gif'.

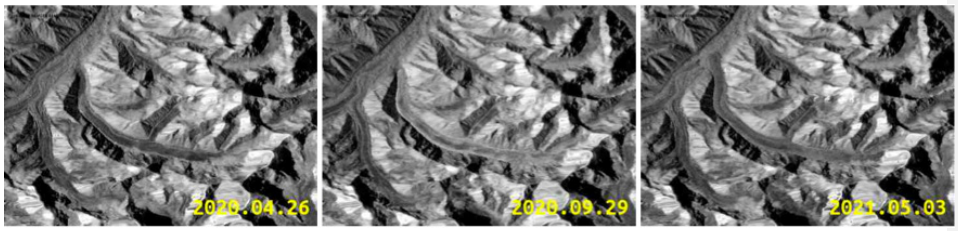

Figure SA: Sentinel-1 multi-looked backscattering intensity images of South Chongtar Glacier for (a) 26.4.2020, (b) 29.9.2020 and (c) 3.5.2021. The time series and the image extracts shown above contain modified Copernicus Sentinel-1 data 2020/21.